Hydrodynamic coefficients from forced and decay heave motion tests of a scaled model of a column of a floating wind turbine equipped with a heave plate

Antonio Medina-Manuel [a], Elkin Botia-Vera [a], Simone Saettone [a], Javier Calderon-Sanchez [b], Gabriele Bulian [c], Antonio Souto-Iglesias [b,*]

[a] CEHINAV, ETSIN, Universidad Politécnica de Madrid (UPM), Madrid, Spain
[b] CEHINAV, DACSON, ETSIN, UPM, Madrid, Spain
[c] Department of Engineering and Architecture, University of Trieste, Via A. Valerio 10, 34127, Trieste, Italy

ARTICLE INFO

Keywords:
Heave motion
Decay tests
Forced oscillation tests
Damping
Added mass
Floating wind turbine

ABSTRACT

This paper describes the results of an experimental campaign aimed at the determination of heave hydrodynamic coefficients for a column of a floating wind turbine platform, equipped with a solid heave plate. The tests are carried out with an experimental system that allows performing both heave forced oscillation tests and heave decay tests. A specific characteristic of the system is the reduced mechanical friction, thanks to the use of air bushings. A series of forced oscillation and decay experiments have been carried out with such a model, and the hydrodynamic coefficients obtained in both types of tests are compared. Results show correlation between both methods if the mean of the peaks of the decay process is chosen to represent its Keulegan–Carpenter number (KC), with a fair matching of the results in the KC range where both methods are applicable. With the objective of conducting an uncertainty assessment which can be relevant for the full-scale extrapolation of results, non-dimensional added mass and damping coefficients are proposed. They incorporate the primitive relevant variables and are shown to lead to a notable collapse of the various results in the form of curves with small differences among them. With these coefficients, an uncertainty assessment is carried out, propagating to those coefficients the uncertainties of the primitive variables in place. Such non-dimensional coefficients are useful to develop simple models to estimate the dimensional ones to be used in numerical simulations of the full scale system. The estimated uncertainties can serve to define design safety margins for the values of such coefficients.

1. Introduction

Experimental investigations have been important for the improvement of floating wind turbines (FWTs) in moored conditions (Gueydon and Weller, 2013; Goupee et al., 2014; Simos et al., 2018) and in the form of decay and forced oscillation tests. Both types are necessary for obtaining data to calibrate numerical models of such floaters (Tao and Dray, 2008; Li et al., 2013; Thiagarajan and Moreno, 2020; Lopez-Pavon and Souto-Iglesias, 2015; Liu et al., 2021).

Decay tests allow to estimate the natural periods and hydrodynamic coefficients (added mass and damping) in resonance conditions (Bachynski and Moan, 2012; Simos et al., 2018; Uzunoglu and Guedes Soares, 2020; Liu et al., 2018). Forced oscillation tests complement decay tests when those coefficients display a significant frequency dependence.

Heave forced oscillation tests carried out with scaled models of FWT and other offshore systems are often performed with a system consisting of a single or more linear actuators, guides and bearings (see, e.g., Tao and Dray (2008), Li et al. (2013), Wadhwa et al. (2010) and Mentzoni and Kristiansen (2020)). These systems restrain all degrees of freedom (DoFs) except the vertical one.

Decay tests are usually conducted by shifting the floater from its equilibrium position in the degree of freedom of interest. When released, the floater starts to oscillate with its natural period in that degree of freedom. With such procedure, since the other degrees of freedom are not restrained, one finds that some of them may be excited, thus implying that kinetic energy from the degree of freedom of interest is transferred to these others, a fact which may reduce the accuracy of the results obtained with such a method. As a matter

* Corresponding author.
E-mail address: antonio.souto@upm.es (A. Souto-Iglesias).

Accepted 26 February 2022

of fact, Bezunartea-Barrio et al. (2019) and do Carmo et al. (2020) reported significant differences between the hydrodynamic coefficients estimated by performing heave forced oscillation and decay tests for free-floating models. The former suggested that such differences could be partially explained by the energy dissipated through pitch and roll motion excitation during the heave decay experiments.

This coupling with other degrees of freedom during heave decay tests could be prevented by developing a system capable of conducting both forced oscillation tests and decay experiments while restraining the motion to the degree of freedom of interest. One aim of this paper is to present and describe a novel system of this type. Results from both types of tests, using a model scale leg of a semi-submersible wind turbine, are presented as a proof of concept of the developed device, being useful as well to investigate the correlation of the values of hydrodynamic coefficients obtained from both methods.

Finally, it is important to report the results from an experimental study with an accompanying measure of the associated uncertainty. Generally speaking, according to ITTC (2014a), the concept of uncertainty can be related with the 'truthfulness' of a measured value. The 'true value' of a quantity subject to measurement may never be known, due to the intrinsic limitations of the measurement procedure. Therefore, the uncertainty associated with a measured quantity is meant to provide a quantitative measure reflecting the level of measurement error as well as, more generally, the limited knowledge of some relevant parameters in the experimental procedure. Thus, according to ITTC (2014a), the result of a measurement can be regarded as complete only when it is accompanied by a quantitative statement of associated uncertainty. In the present research, due the lack of literature on specific procedures for the problem in hand, the experimental uncertainty assessment is conducted in accordance with the ITTC general principles (ITTC, 2014a).

The paper is organized as follows. A hydrodynamic model, particularized for both type of tests, is first presented. The novel proposed system is then described, including its main elements. The specimen used for the proof-of-concept, the tests carried out, the associated results and their uncertainty assessment are finally discussed.

2. Hydrodynamic model

2.1. General

Eq. (1) shows the classic hydrodynamic model used for these experimental studies, when the information obtained from them is to be used in frequency domain analysis.

$$M\ddot{z} = -A_{33}\ddot{z} - B_{33,eq}\dot{z} - C_{33}z + F_{ext}, \tag{1}$$

where $z(t)$ is the vertical position, M is the model mass, F_{ext} is the actuator force (measured with a load cell), A_{33} is the added mass, $B_{33,eq}$ is the equivalent linear damping, and C_{33} is the static restoring in heave motion.

A quadratic model for the damping could be considered if we are interested in time domain modelling. In order to keep the length of present paper reasonable, this is left, however, for future work.

The external forces due to air resistance and air bushings friction are considered negligible in the present research.

2.1.1. Forced oscillation tests analysis

For forced oscillations, the position $z(t)$ is modelled, after removing the initial transient, as:

$$z(t) = z_0 \cos(\omega \cdot t), \tag{2}$$

where z_0 is the motion amplitude and ω its oscillation frequency.

The hydrodynamic force in Eq. (1) can be estimated as:

$$F_H(t) = -A_{33}\ddot{z} - B_{33,eq}\dot{z} = -F_{ext} + M\ddot{z} + C_{33}z. \tag{3}$$

The time history of the hydrodynamic force $F_H(t)$ from one forced oscillation sample experiment can be seen in Fig. 1. This time history is presented in non-dimensional form as a force coefficient:

$$C_F(t) = \frac{F_H(t)}{1/2\rho\ (\omega\ z_0)^2\ S}, \tag{4}$$

where S is the frontal area of the body during heave motion ($S = \pi D_d^2/4$ in the case of the body having a circular heave plate with diameter D_d).

Both A_{33} and B_{33} are obtained directly from Eq. (3) by decomposing the first harmonic hydrodynamic force, F_H, into its phase and counter-phase components, assuming harmonic motion according to Eq. (2). If Eq. (3) is multiplied by $\dot{z}(t)$ and integrated over one period, B_{33} is the only term left in the projection (Garrido-Mendoza et al., 2015):

$$B_{33} = -\frac{\int_t^{t+T} F_H(t)\cdot\dot{z}(t)\,dt}{\int_t^{t+T}\dot{z}^2(t)\,dt} \tag{5}$$

The same process is done for A_{33}, but multiplying by $\ddot{z}(t)$:

$$A_{33} = -\frac{\int_t^{t+T} F_H(t)\cdot\ddot{z}(t)\,dt}{\int_t^{t+T}\ddot{z}^2(t)\,dt} \tag{6}$$

The obtained added mass and damping are made non-dimensional as Tao and Dray (2008):

$$A'_{33} = \frac{A_{33}}{A_{33,th}}, \tag{7}$$

$$B'_{33} = \frac{B_{33}}{\omega A_{33,th}}, \tag{8}$$

where $A_{33,th}$ is the theoretical added mass (see Eq. (24)).

Other non-dimensional parameters relevant in the present analysis are:

- The frequency parameter, β:

$$\beta = \frac{D_d^2 f}{\nu}, \tag{9}$$

  with f the frequency in Hz and ν the kinematic viscosity of water.
- The Keulegan–Carpenter number, KC:

$$KC = 2\pi\frac{z_0}{D_d}. \tag{10}$$

- The Reynolds number, Re:

$$Re = KC\cdot\beta. \tag{11}$$

2.1.2. Decay tests analysis

The treatment of the decay experiments analysis is different from forced oscillation ones. For each forced oscillation test with a certain frequency and amplitude, a single added mass and a single damping coefficient are obtained. However, for each decay experiment, several coefficients could be computed. The initial transient cycles and the last cycles of each experiment are discarded. Then the analysis is done half cycle by half cycle. A similar analysis is done in roll decay tests (Bulian et al., 2009). Fig. 2 illustrates one decay sample with the part used to study and its peaks.

Decay experiments are analysed by assuming that the measured data of each half heave cycle can be approximated to the theoretical solution of a damped single DoF system. The equation responds to the hydrodynamic force model presented in Eq. (1). In this case, the actuator force is zero, and the equation of motion can be written as:

$$\ddot{z} + 2\mu_{eq,i}\dot{z} + \omega_{3,eq,i}^2\ z = 0, \tag{12}$$

where the equivalent linear damping coefficient is

$$\mu_{eq,i} = \frac{B_{33,eq,i}}{2\cdot(M + A_{33,i})}, \tag{13}$$

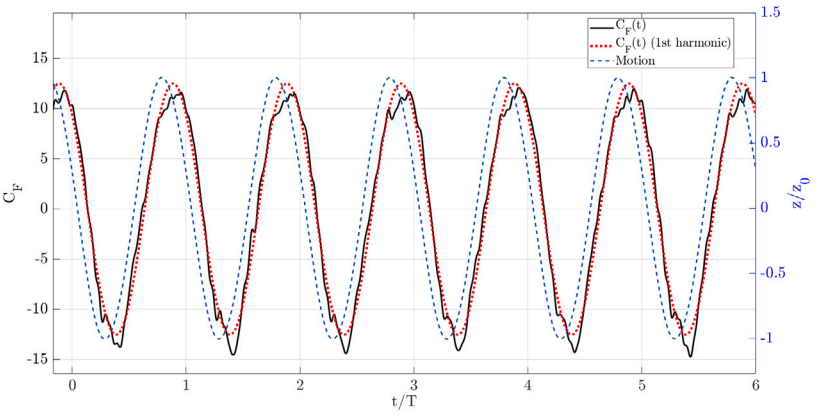

Fig. 1. Hydrodynamic force coefficient time history, $C_F(t)$, Eq. (4), measured in one sample experiment: $T = 11.2$ s, $KC = 0.628$.

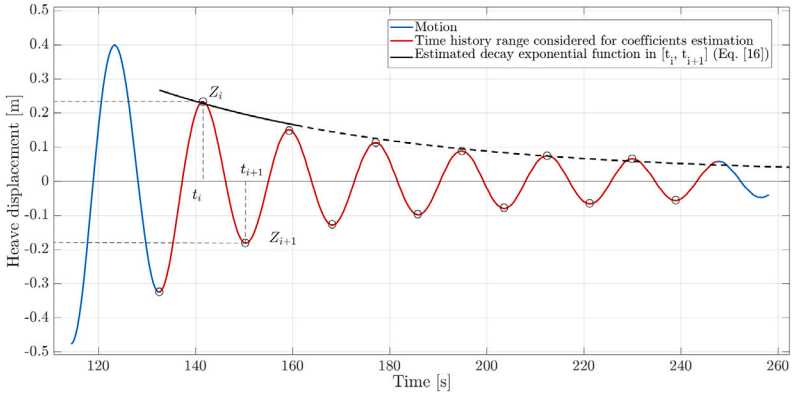

Fig. 2. Decay motion time history measured in one sample experiment in full scale. Initial $KC = 0.157$.

and the equivalent undamped natural frequency is

$$\omega_{3,eq,i} = \sqrt{\frac{C_{33}}{M + A_{33,i}}}. \tag{14}$$

Both are assumed to vary slowly across the decay cycles. The sub-index i refers to the ith-half cycle, starting at time t_i in a local extreme (see Fig. 2).

According to Eq. (12), and with the following notation:

$$\forall i \quad z\left(t_i\right) = Z_i, \ \dot{z}\left(t_i\right) = 0, \tag{15}$$

the heave decay for the ith-half cycle can be approximated, assuming that the system is lightly damped, by the following analytical solution:

$$z(\tau) = e^{-\mu_{eq,i}\cdot\tau} Z_i \cos(\omega_{3,d,i} \cdot \tau), \tag{16}$$

with $\tau = t - t_i$ and the damped natural frequency

$$\omega_{3,d,i} = \sqrt{\omega_{3,eq,i}^2 - \mu_{eq,i}^2}. \tag{17}$$

If there is no coupling between the different DoFs, the damped natural frequency is determined approximately from the time between consecutive peaks:

$$\omega_{3,d,i} = \frac{\pi}{t_{i+1} - t_i}. \tag{18}$$

By taking logarithms of Eq. (16) for two consecutive peaks in the time interval $[t_i, t_{i+1}]$, the characteristic parameter $\mu_{eq,i}$ is given by:

$$\mu_{eq,i} = \frac{1}{t_{i+1} - t_i} \log\left(\frac{|Z_i|}{|Z_{i+1}|}\right). \tag{19}$$

Considering that the reduction $|Z_i| - |Z_{i+1}|$ of the heave envelope is sufficiently small (lightly damped), it is possible to associate $\mu_{eq,i}$ and $\omega_{3,d,i}$ to the mean of $|Z_i|$ and $|Z_{i+1}|$, denoted by $\tilde{z}_i$, for the ith-half cycle, which gives us the KC_i values presented in Section 6. Once these characteristic parameters are determined, added mass and damping can be obtained as follows for each KC_i:

$$A_{33,i} = A_{33}\left(\tilde{z}_i\right) = \frac{C_{33}}{\omega_{3,eq,i}^2} - M, \tag{20}$$

and the total dimensional damping:

$$B_{eq,33,i} = B_{eq,33}\left(\tilde{z}_i\right) = 2\eta_i \sqrt{\left(M + A_{33,i}\right) C_{33}}, \tag{21}$$

with $C_{33} = \rho\, g\, S_w$, where S_w is the waterplane area, g is the gravity constant and ρ is the water density. The non-dimensional damping η_i is obtained as:

$$\eta_i = \eta\left(\tilde{z}_i\right) = \frac{\mu_{eq,i}}{\omega_{3,eq,i}}. \tag{22}$$

The non-dimensional damping η_i is defined here as a fraction of the critical damping B_{33}^{crit}, which is the damping coefficient above which free decays no longer show oscillatory behaviour. The critical damping can be determined as:

$$B_{33,i}^{crit} = 2\sqrt{(M + A_{33,i})C_{33}}. \tag{23}$$

For the decay tests, the hydrodynamic coefficients are presented in their non-dimensional form as in forced oscillation tests (see Eq. (7) and (8)).

Depending on the particular cycles used, the hydrodynamic coefficients may vary. In the present work, as aforementioned, Bulian et al. (2009) has been followed, discarding the initial transient part. This implies that the KC representative values of the decay tests are lower than the forced oscillation ones, despite starting both tests with the same initial amplitude.

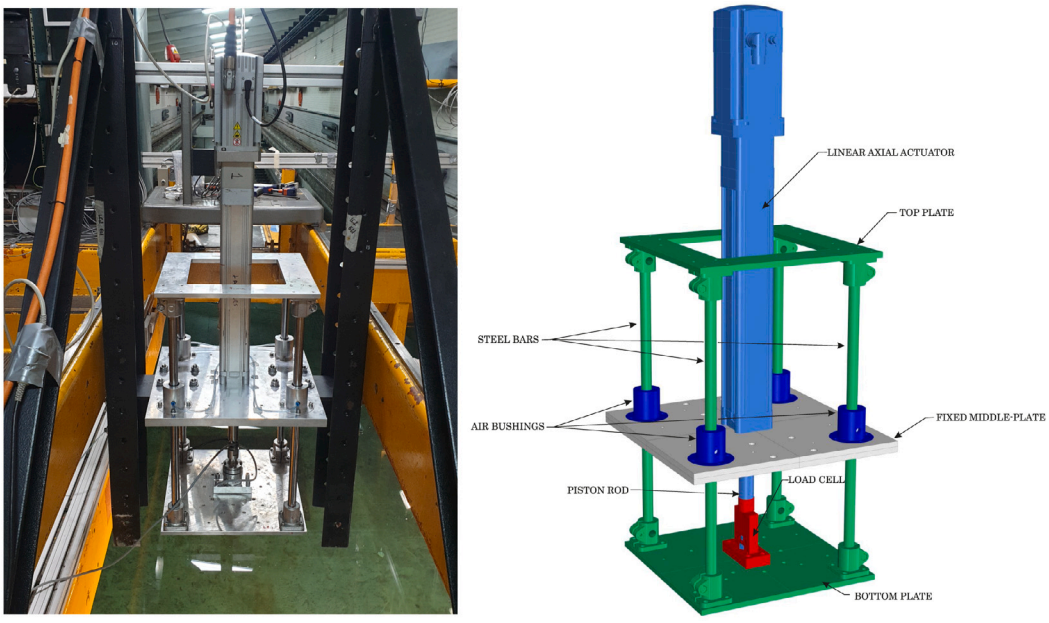

Fig. 3. Picture of the developed system (left). The actuator is attached to the system through a single DoF load cell. Parts of the developed system (right).

3. Experimental device

Fig. 3 shows the system developed as part of the present research. It consists of a moving frame and a fixed part. The moving frame (green coloured in Fig. 3) includes four steel bars that connect a lower and an upper plate. The bottom plate is attached to the model. The intermediate fixed clamped plate (grey coloured in Fig. 3), wherein the bars oscillate, has an opening for inserting the actuator (light blue coloured in Fig. 3) and incorporates four air bushings (dark blue coloured in Fig. 3) used to reduce the friction caused by oil-lubricated bearings. The actuator is connected to the bottom plate through a load cell (red coloured in Fig. 3). The moving frame is set in motion by the actuator in the case of forced oscillation experiments. For decay tests, the actuator is detached from the bottom plate so that the system can oscillate freely.

The moving part is fabricated in aluminium to minimize its weight (10.488kg). Therefore, the system is suitable for free-decays with models whose difference between displacement and weight is larger than this value.

The entire system is attached to the towing tank carriage, which provides a robust and fixed reference, and which allows testing in any longitudinal position of the basin, even while moving at certain speeds. The authors designed a frame (black beams in the left panel of Fig. 3) with several possible vertical positions to be clamped to the towing carriage. This frame allows to change the relative position between the model and the water surface. The fine tuning (±1 mm) is achieved by changing the filling level in the tank. Two diagonal reinforcements are added to increase the stiffness of this main frame. A wider perspective of the system can be seen in Fig. 4.

These characteristics make the designed system suitable for both decay and forced oscillation tests with negligible friction and with only the heave degree of freedom. A dedicated appendix, Appendix A, presents the technical characteristics of the various parts of the system. Supplementary multimedia files are provided with this article. Videos of the system in operation during forced oscillation experiments and decay tests are available from http://canal.etsin.upm.es/papers/medinamanueletal2021/.

4. The specimen

As a proof of concept of the system, and in order to investigate the relationship between hydrodynamic coefficients obtained with forced oscillation and decay tests, a battery of tests was carried out. The specimen used is the scaled model (1:20 scale) of one leg, equipped with a plain heave plate, of a semi-submersible floating wind turbine design whose hydrodynamic coefficients were studied by Lopez-Pavon and Souto-Iglesias (2015) and Bezunartea-Barrio et al. (2019), and its related vortex shedding by Anglada-Revenga et al. (2020) and Saettone et al. (2021), both when subjected to forced heave motions.

The main dimensions of the leg, including the disc, are presented in Fig. 5 and Table 1 in full and model scale. In Table 1, the platform draft is measured to the bottom of the heave plate. Fig. 5 also presents a sketch of the transverse section of the tank.

5. The tests

5.1. General

All tests presented in this article have been performed in the towing tank of ETSIN-UPM, whose dimensions are:

- Length: 100 m.
- Breadth: 3.8 m.
- Depth in the current experiments: 2.2 m.

The most restrictive dimension was, in this case, the breadth of the tank. Some spurious lateral resonance effects might occur when the propagation velocity of the waves generated is such that they reflect off the tank walls and reach the leg synchronized with the motion period (Lopez-Pavon and Souto-Iglesias, 2015). Following the dispersion relationship and assuming water depth effects negligible, this effect was expected for a model scale period $T \approx 1.56$ s. This will be further discussed in the Results section of this paper.

It is also remarked that similar, and actually further confined configurations were used in past experiments by other researchers, e.g. (Tao and Dray, 2008; Wadhwa et al., 2010). However, apart from the comments by Wadhwa et al. (2010) indicating that some corrugations had been included in order to try to mitigate these effects, no mention to any significant spurious effects from wave reflection has been found in literature. Finally, the ratio, h/r_d, is large (1.53, see Table 1), thus implying that the flow will hardly be influenced by the free surface, as justified by Lopez-Pavon and Souto-Iglesias (2015) with the same configuration used in present work.

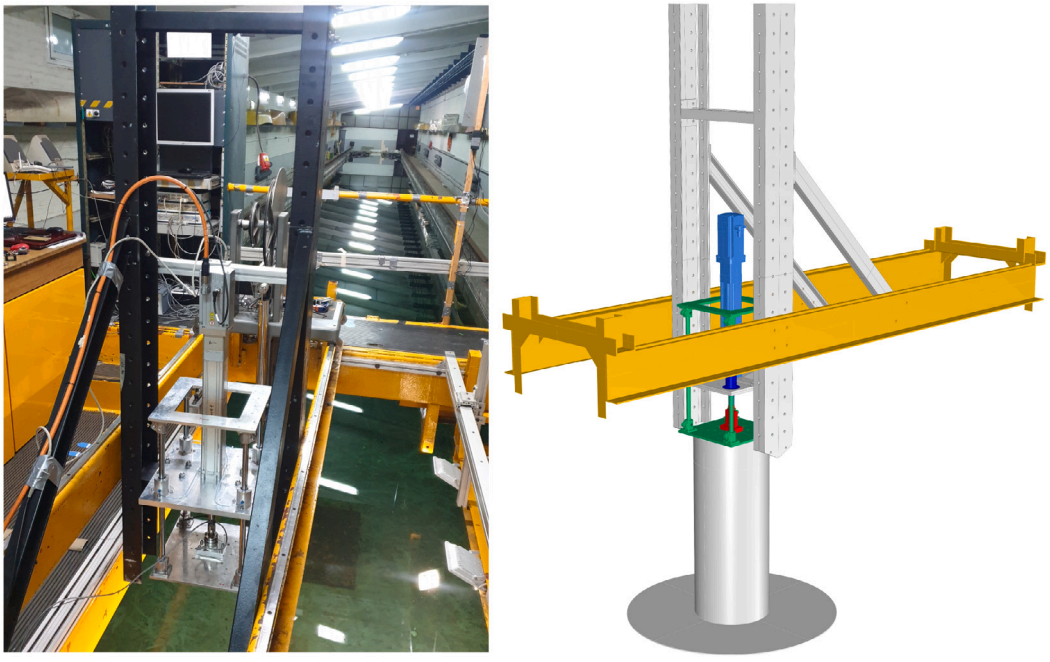

Fig. 4. Left panel: entire set up in forced oscillation tests with the model. Vertical points on beams provide freedom to position the model with respect to the tank free surface. Right panel: Yellow horizontal beams represent the tank carriage beams. (For interpretation of the references to colour in this figure legend, the reader is referred to the web version of this article.)

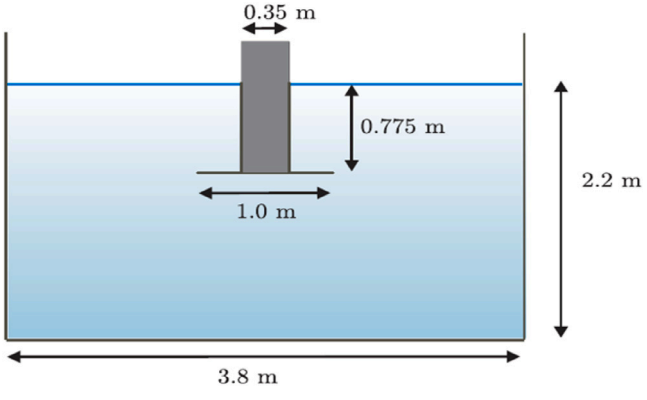

Fig. 5. Model with heave plate disc configuration and its main dimensions. Location and set-up in the tank. The model is placed in the centre of the tank.

Table 1
Main model dimensions.

Characteristic	Symbol	Prototype	Model
Platform draft, disc depth	h	15.5 m	0.775m
Column diameter	D_c	7.1 m	0.355 m
Heave plate (disc) diameter	D_d	20 m	1.0 m
Heave plate (disc) radius	r_d	10 m	0.5 m
Heave plate (disc) thickness	t_d	0.1 m	5 mm
Disc aspect ratio	t_d/D_d	0.005	0.005
Depth-radius ratio	h/r_d	1.55	1.55
Column mass	M	663 t	82.83 kg
Disc distance to the tank bottom	h_b	28.5 m	1.425 m
Disc distance to the bottom-radius ratio	h_b/r_d	2.85	2.85

Regarding eventual bottom effects, the ratio between the distance to the bottom and the disc radius, h_b/r_d, is 2.85. According to the numerical analysis in (Garrido-Mendoza et al., 2015), the effect of the bottom on the heave plate flow is, for these conditions, negligible. Fig. 6 illustrates the entire setup in forced oscillation tests with the model attached.

5.2. Test matrix

5.2.1. Forced oscillation tests

Vertical oscillations tests were performed with five different KCs (0.078; 0.157; 0.314; 0.628; 0.866) and a range of different frequencies $\omega/\omega_{3,th}$ (1 −4.47), with $\omega_{3,th}$ being the theoretical heave natural frequency (see Eq. (25) later in the paper). For each frequency, the maximum feasible amplitude depends on the actuator power, leading to higher oscillation frequencies for the smallest motion amplitudes. Some points close to the tank lateral resonance were added to see the effects of conducting tests in restricted lateral conditions. Five repetitions were done for each KC and different frequencies in order to conduct uncertainty analysis (see Appendix B).

5.2.2. Decay tests

Decay tests were performed starting from the same range of initial amplitudes tested with forced oscillation tests, leading to the same initial KCs. For each test, three repetitions were done to conduct uncertainty analysis (see Appendix C).

6. Results

6.1. Forced oscillations

The added mass and damping coefficients presented herein are made non-dimensional according to Eqs. (7) and (8), for which the theoretical added mass, $A_{33,th}$, is needed. Following Sarpkaya and Isaacson (1981), the theoretical added mass of a thin disc oscillating

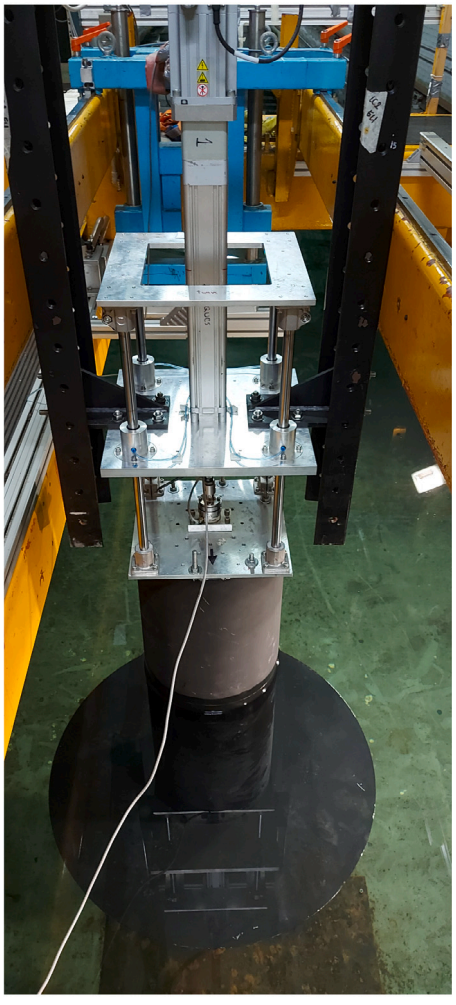

Fig. 6. Set up for forced oscillation tests, with the model attached to the system.

perpendicular to its plane in ideal flow in the low KC limit can be approximated by:

$$A_{33,th} = \frac{1}{3}\rho D_d^3 \tag{24}$$

This theoretical added mass can be corrected to account for the cylindrical column volume, as in Ref. (Tao et al., 2007), yielding a reduction of around 10% (from 333 to 303 kg, at scale 20). The difference is considered large enough so as to maintain this corrected value as the reference one.

Results discussed herein are presented as a function of KC. They were obtained as discussed in Section 2.1.1. In Figs. 7 and 8, the coefficients A'_{33} and B'_{33} for the studied conditions are shown. On the one hand, a weak dependence between hydrodynamic coefficients and the β values (frequency dependence), can be observed. On the other hand, a strong dependence of the coefficients on KC (oscillation amplitude) is noticeable. For these reasons, five repetitions were done for each KC but not for all β. The size of the error bars is taken as the standard deviation σ of the experiments carried out for each amplitude. They are too small to be appreciated in the figures as in terms of relative errors they are all below 2%.

Both A'_{33} and B'_{33} follow a linear or quasi-linear trend with KC. It can be appreciated that for $\beta = 640753$ and 664709, the curves do not follow the same tendency. The reason is attributed to the fact that these frequency parameter values are close to the ones that correspond to the lateral resonance frequency of the tank, discussed in Section 5.

6.2. Decay tests

The theoretical heave natural frequency $\omega_{3,th}$ at model scale can be computed as:

$$\omega_{3,th} = \left(\frac{\rho\ g\ S_w}{M + A_{33th}}\right)^{0.5} = 1.57 \text{ rad/s}. \tag{25}$$

The corresponding prototype period is 17.9 s, which is above common operational first order excitations. When decay tests were performed, a natural period at prototype scale of 17.85 s was found, close to the theoretical one.

Results from decay tests are presented in Figs. 9 and 10. The coefficients have been obtained as discussed in Section 2.1.2. The selection of a representative value of KC is a somewhat arbitrary aspect to be set in decay tests since the motion amplitude diminishes over time. For the current analysis, the representative KCs are the mean, $\tilde{z}_i$, of the peaks of the heave time history of each half cycle (see Fig. 2), leading to a set of several values for each experiment. As it is done in roll decay analysis (Bulian et al., 2009) the initial transient cycles and the last ones are removed from the analysis since they render inconsistent results.

As can be seen in Figs. 9 and 10, both added mass and damping coefficients increase linearly with the amplitude, similarly to forced oscillation tests.

As done in forced oscillation tests, repetitions for each experiment were done. Furthermore, both starting up and starting down initial motion amplitudes were tested in these free decay experiments. Assuming an increasing linear trend of the hydrodynamic coefficients with KC, Figs. 9 and 10 present the error bars as the standard deviation of residual values from the trend displayed obtained with a least squares fitting.

A comparison between decay and forced results is presented in Figs. 11 and 12. Since the initial transient part in free decay is discarded in the analysis, the representative amplitude values for decay tests are lower than forced oscillation tests, as shown in the figures. However, there is a sufficient overlapping of the lowest values from forced oscillation tests and the highest ones found from decay experiments.

The correlation between the added mass coefficients found in forced oscillation and decay tests is noticeable. The damping results show continuity with the results from forced oscillation but the trends are different, with the decay tests values displaying a steeper decrease as the KC goes to zero. To the authors' knowledge this type of comparative analysis between forced oscillation and decay tests had not been previously documented in the literature.

One has to bear in mind that the hydrodynamics during the decay tests and periodic forced oscillation tests are, in principle, different. In decay tests, the intensity of the vorticity field diminishes during consecutive cycles, thus reducing the possibility of strong cycle to cycle interactions. In forced oscillation tests, the vortical structures may stay close to the structure from one cycle to the next, which allows interactions between vortices. This factor may partially explain the differences found between the coefficients obtained with decay and forced oscillation tests.

A wider overlapping range of KC would be desirable. However, this overlapping range is not wider because, first, the maximum representative KC for decay tests is limited by the specifications of the experimental system, by the existence of an initial transient part not accounted for in the analysis, and by the large intrinsic damping of this particular floater, which leads to a steep decay of the motion amplitudes.

Second, the overlapping range is not wider because the minimum KC for heave oscillation tests is limited due to the fact that for low KCs the measured hydrodynamic force will be much smaller than the restoring force, a fact that makes it unfeasible to measure the former accurately, as it has to be obtained by subtracting the latter much larger component from the experimental register.

Overall, the reported observations support the importance of assessing the suitability of experimental approaches combining free decays and forced tests.

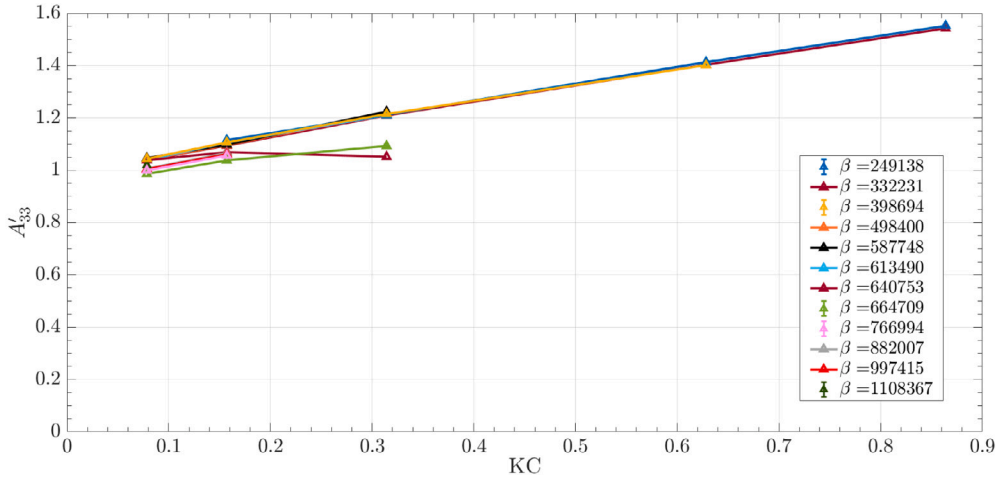

Fig. 7. Forced oscillation tests: added mass coefficient.

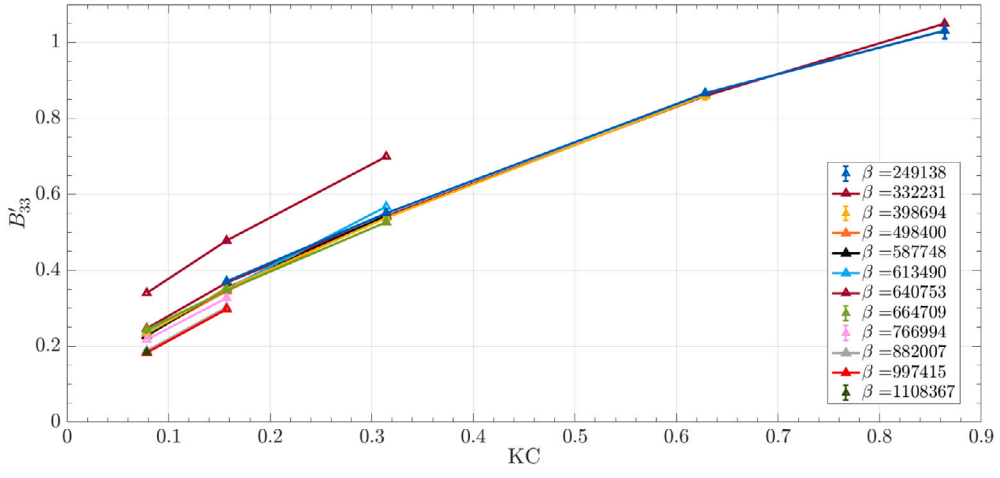

Fig. 8. Forced oscillation tests: damping coefficient.

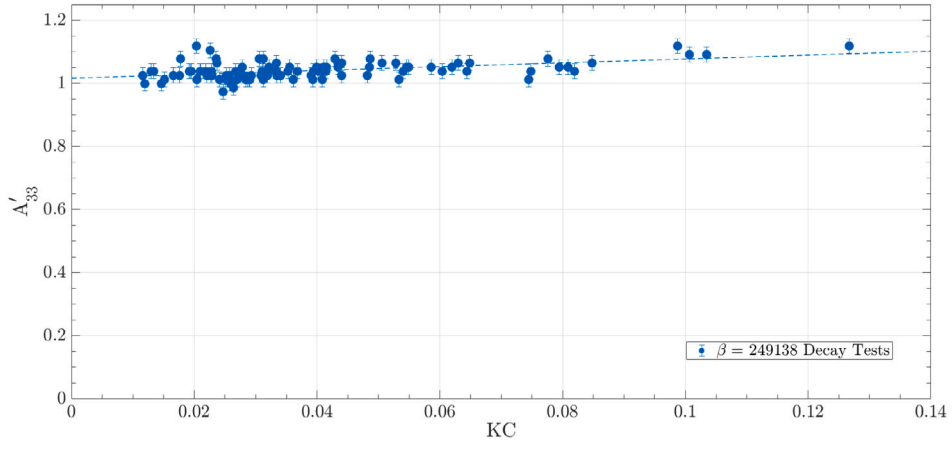

Fig. 9. Decay tests: added mass coefficient.

7. Modified hydrodynamic coefficients for propagation of experimental uncertainties

7.1. General

It is not innocent that the error bars presented for forced oscillation tests in Figs. 7 and 8 are strictly linked to repeatability (and dispersion) of the experimental measurements and have been measured as the standard deviation of the samples. Such bounds are informative but insufficient to characterize the actual uncertainty (confidence interval of the mean of the measured values), which requires accounting for the influence of the such repeatability of the measured data, but also the uncertainties related to the elements and variables involved in the

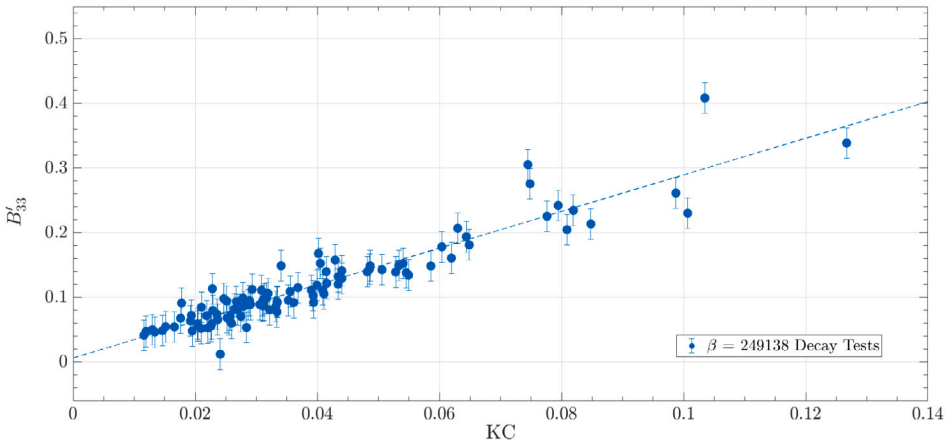

Fig. 10. Decay tests: damping coefficient.

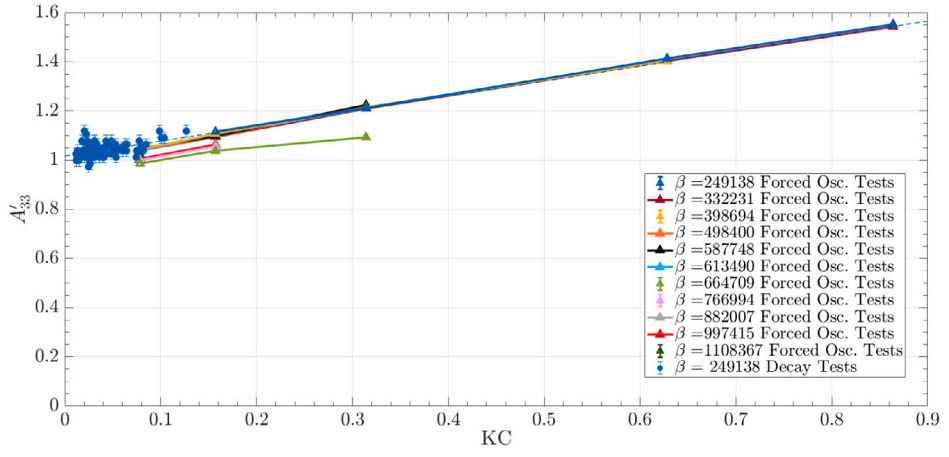

Fig. 11. Forced oscillation and decay tests: added mass coefficient.

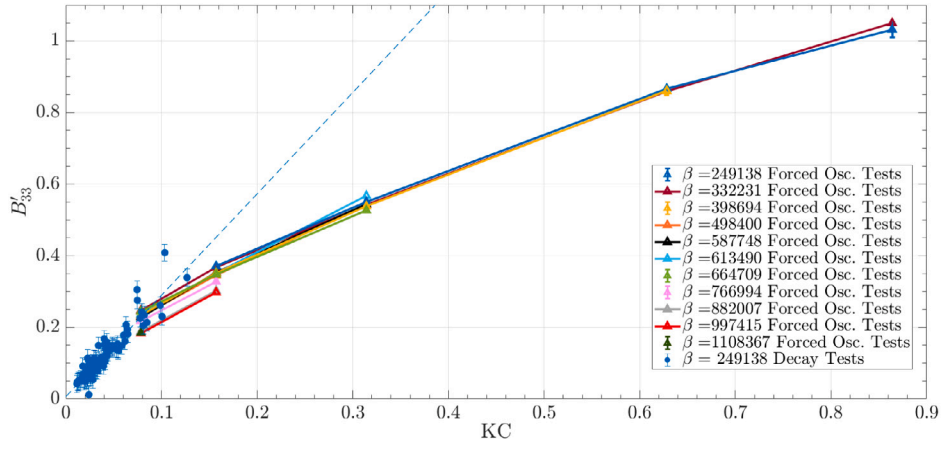

Fig. 12. Forced oscillation and decay tests: damping coefficient.

experiments (specimens, motion amplitude, frequency, force, etc.), and the precision of the measurement equipment.

Moreover, it is important to highlight that the actual goal of any of these tests is to provide information that can be used for full scale prototypes.

Considering both matters (influence of other aspects on top of the repetition in uncertainty, and the impact of such uncertainties in full scale extrapolations), non-dimensional coefficients are proposed in this section that can be used for extrapolation of the added mass and damping to full scale and whose uncertainties can reflect both the repeatability related uncertainties and those due to the input data and measuring equipment precision.

There is not much literature available regarding experimental uncertainty on the hydrodynamics of floating wind energy devices. Robertson et al. (2020) assessed whether the uncertainty of the second order effects measured in experiments for moored configurations could explain the deviations with respect to a number of numerical models. This work had as a precursor a previous one co-authored by these

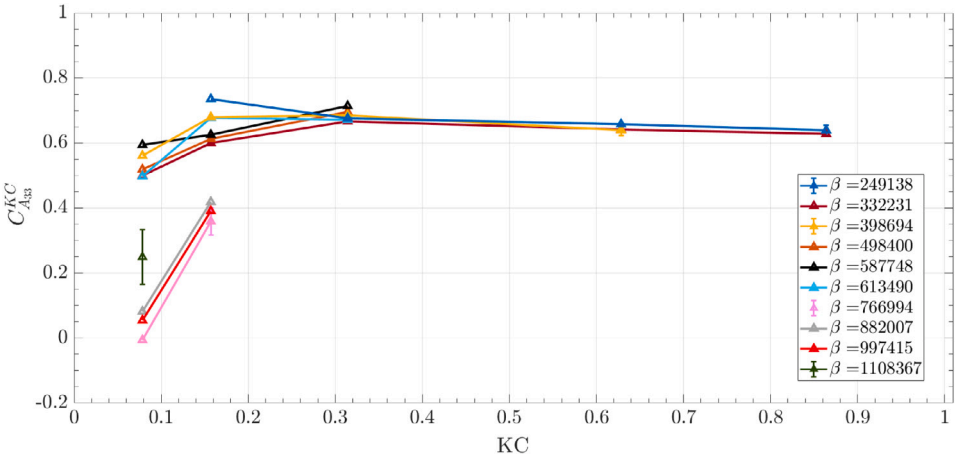

Fig. 13. Forced oscillation tests: modified added mass coefficient, $C^{KC}_{A_{33}}$, Eq. (27).

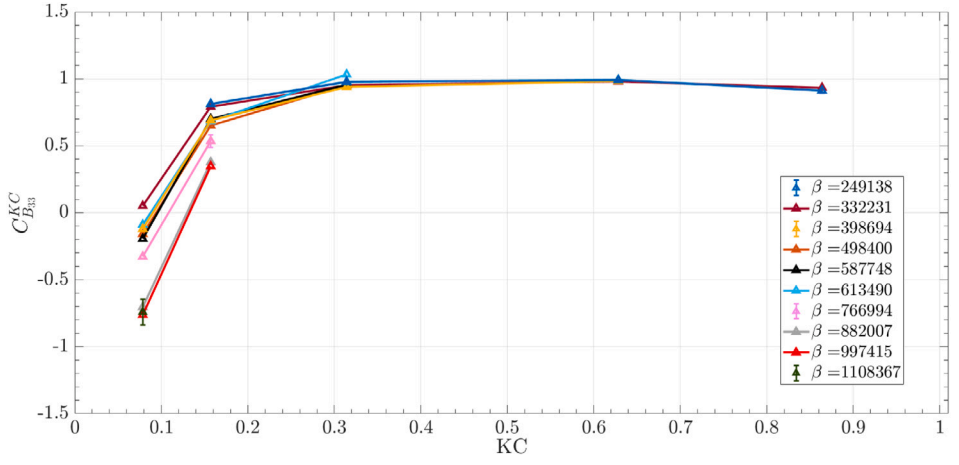

Fig. 14. Forced oscillation tests: modified damping coefficient, $C^{KC}_{B_{33}}$, Eq. (28).

authors (Robertson et al., 2018), in which the main sources of uncertainty in moored floater seakeeping experimental campaigns had been identified.

However, the present work focuses on forced oscillation and decay tests, for which no uncertainty assessment is found in literature. For this reason, the present analysis is herein conducted in accordance with the ITTC general principles in (ITTC, 2014a). According to such principles, the dimensional total uncertainty, $u(f)$, of a variable of interest, f, is obtained by propagating those of the n identified variables, x_i, affecting the referred variable of interest, $u(x_i)$. Under the assumption that the variables x_i are uncorrelated:

$$u(f)^2 = \sum_{i=1}^{n} \left(\frac{\partial f}{\partial x_i} u(x_i) \right)^2 . \tag{26}$$

It has been shown in the paper that the hydrodynamic coefficients display a weak dependence on oscillation frequency but a quasi-linear one on the KC number. For this reason, in order to incorporate the uncertainty in KC in the model, we propose non-dimensional variables built as ratios making use of the hydrodynamic coefficients A'_{33} and B'_{33} (Eqs. (8), (7)), and the KC number:

$$C^{KC}_{A_{33}} = \frac{A'_{33} - 1}{KC} = \frac{1}{KC} \left(\frac{A_{33}}{A_{33th}} - 1 \right), \tag{27}$$

$$C^{KC}_{B_{33}} = \frac{B'_{33} - B'_{330}}{KC} = \frac{1}{KC} \left(\frac{B_{33} - B_{330}}{\omega\, A_{33th}} \right). \tag{28}$$

In the case of the added mass coefficient, one is subtracted from the numerator as the theoretical low KC limit is one for the A'_{33} ratio. Regarding the damping coefficient, as can be appreciated in Fig. 8, it does not tend to zero as KC tends to zero, but a small offset, of the order of 0.2 (obtained by fitting a least-squares straight line at the largest KC range in forced oscillation tests) is noticeable. Such offset has been attributed in the literature to viscous friction effects, connecting it to Stokes' oscillating plate second problem (Thiagarajan and Troesch, 1994; Garrido-Mendoza et al., 2015). This offset was also described (with a similar value) in a previous set of tests with this model and smaller geometrically similar ones (Bezunartea-Barrio et al., 2019) in a different facility. Let us treat that offset as a constant and denote it as B'_{330} (B_{330} in its dimensional form).

Since, as discussed in the previous section, the dependency on β of the values obtained is small, β has not been included as part of these proposed coefficients.

Figs. 13 and 14 show the trend of these proposed coefficients. The curves corresponding to β values affected by the lateral tank sloshing effect have been removed. Overall, as can be appreciated, the curves collapse rather fairly to constant values, as a consequence of their quasi-linear behaviour and the chosen non-dimensionalization.

For the added mass, the coefficient tends to a value around 0.6 for large KC, $C^{KC}_{A_{33\infty}} \approx 0.6$, which implies that a practical estimate could be

$$A_{33} \approx A_{33th}\,(1 + 0.6\ KC)\,. \tag{29}$$

The dispersion of the values for low KCs is explained by the associated larger uncertainties (the uncertainty bars are included in the graph and

will be discussed next) and to other effects whose interpretation is left for future work, but that basically are connected to the fact that the low KC limits are not constant across all the β – constant curves.

For the damping coefficient, the modified coefficient tends to a value around one for large KC, $C^{KC}_{B_{33\infty}} \approx 1$, which implies that a practical estimate could be:

$$B_{33} \approx B_{330} + \omega\, A_{33th}\, KC. \tag{30}$$

The same comments regarding the dispersion of the values for low KCs made for the added mass coefficient apply also to this modified damping coefficient.

The uncertainty bars presented in Figs. 13 and 14 are the total expanded uncertainties computed as described thoroughly in Appendix B. They are included for a large number of forced oscillation tests for which repetitions (5) are also available. An in-depth discussion about the absolute values of the uncertainty for both forced oscillation and decay experiments can be found in Appendix B.

7.2. Extrapolation

Considering the work of Bezunartea-Barrio et al. (2019), which shows that scale effects are less important than an accurate choice of the representative KC when it comes to estimate added mass and damping values, one can assume that the KC–modified added mass and damping coefficients (27), (28) can be extrapolated to full scale as functions themselves only of the KC number.

Since KC is the same at model and full scale if geometric similitude is maintained, the values of those coefficients will be the same at model and full scale. From these coefficients, the full scale dimensional values can be directly obtained.

For the same reason, also the uncertainties found in model scale can be directly incorporated as safety margins for dimensional added mass and damping during the design phase since the rest of the parameters (frequency, amplitude, and so on) are exact in the numerical modelling in the design stage of an engineering project.

8. Conclusions

This paper describes the results of an experimental campaign aimed at the determination of heave hydrodynamic coefficients for a column of a floating wind turbine platform equipped with a solid heave plate. The tests were carried out with an experimental system that allows performing both heave forced oscillation tests and heave decay tests. A specific characteristic of the system is the reduced mechanical friction, thanks to the use of air bushings. As a proof of concept of the system and in order to investigate the relationship between hydrodynamic coefficients obtained with both methods, forced oscillations and heave decay experiments have been conducted.

The hydrodynamic coefficients found in both types of experiments have been compared. Both forced oscillation and decay results overlap in the common Keulegan–Carpenter number (KC) range if the mean of the peaks of the decay process is chosen to represent the KC. This overlapping had not been, to the authors' knowledge, found in the previous experimental literature for this type of tests.

For the forced oscillation tests, the observed tendencies indicate a mostly linear relationship between the hydrodynamic coefficients and KC number. However, for low $KC's$ some frequency dependence has been found.

Regarding the decay tests, the linear tendencies are also clear and the referred overlapping with the forced oscillations values has been found. However, for the very low KCs, where forced oscillation tests are not feasible, the slopes of the curves obtained with decay tests become steeper when compared to that of the forced oscillation tests. Some partial explanations for this behaviour have been proposed.

With the objective of conducting an uncertainty assessment that can be relevant for the full-scale extrapolation of results, modified non-dimensional added mass and damping coefficients have been proposed. They incorporate the primitive relevant variables and lead to a large collapse of the various results in the form of curves with small differences among them. With these modified coefficients an uncertainty assessment has been carried out, propagating to those coefficients the uncertainties of the primitive variables in place. Moreover, simple formulae for estimating the added mass and damping values at full scale have also been proposed, which can be useful for practical industrial applications. The uncertainties obtained can work as safety margins for the values of such coefficients at design stage.

Supplementary data

Supplementary multimedia files are provided with this article. Visit http://canal.etsin.upm.es/papers/medinamanueletal2021/ to watch videos of the system in operation during forced oscillation experiments and decay tests. The data that support the findings of this study are available from the corresponding author upon reasonable request.

CRediT authorship contribution statement

Antonio Medina-Manuel: Conceptualization, Methodology, Investigation, Software, Data Analysis, Writing – original draft, Writing – review & editing. **Elkin Botia-Vera:** Technical assistance. **Simone Saettone:** Writing – review & editing. **Javier Calderon-Sanchez:** Technical assistance. **Gabriele Bulian:** Methodology, Formal Analysis, Writing – review. **Antonio Souto-Iglesias:** Conceptualization, Methodology, Formal Analysis, Writing – original draft, Writing – review & editing, Supervision, Project Administration, Funding acquisition.

Declaration of competing interest

The authors declare that they have no known competing financial interests or personal relationships that could have appeared to influence the work reported in this paper.

Acknowledgements

The authors acknowledge the funding received from the ARCWIND project "Adaptation and Implementation of Floating Wind Energy Conversion Technology for the Atlantic Region (EAPA 344/2016)" which is co-financed by the European Regional Development Fund through the Interreg Atlantic Area Programme. The research was also supported by the Spanish Ministry for Science, Innovation and Universities (MCIU) under grant RTI2018-096791-B-C21 "Hidrodinámica de elementos de amortiguamiento del movimiento de aerogeneradores flotantes". The authors would also like to thank Ricardo Zamora Rodríguez, Juan Luis Chacón and Cristina Romero Monte for their help with various aspects in this initiative.

Appendix A. Components of the experimental device

A.1. Actuator

The actuator is an electromechanical linear axis actuator with a piston rod (model FESTO DNCE 63-300-BS-10-PQ) with a power of 1.3 kW (see Fig. A.15). It is in charge of moving the system to the position $z(t)$ in Eq. (1) with a specified frequency ω.

It is highly accurate in generating the motion, with a precision of $\pm$0.01 mm. Its piston rod, attached to the load cell, connected in turn to the bottom plate, moves the oscillator frame with a maximum working stroke of 300 mm, allowing maximum amplitudes of 150 mm. Regarding the motions, the maximum linear speed is 0.5 m/s. Therefore, with the largest stroke, the highest oscillating frequency is 0.4 Hz. The actuator also includes an encoder that registers the actuator motion during forced oscillation tests. The maximum axial load for this actuator is 2500 N, which is sufficient for the typical models used in the tank.

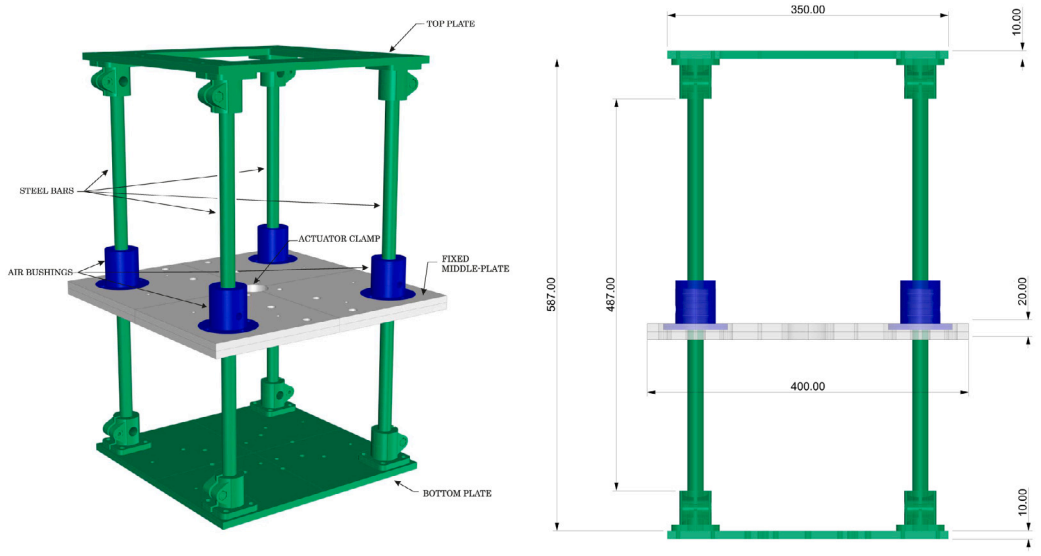

Fig. A.15. Frame parts (left). Bars, bottom and upper plates oscillate (green) while the middle plate stays fixed (grey). Dimensions of the quadrangular plates (right). Units in millimeters. (For interpretation of the references to colour in this figure legend, the reader is referred to the web version of this article.)

A.2. System frame

Three quadrangular aluminium plates form the frame of the novel system (see Fig. A.15). The frame consists of two parts: a moving one (green in the Figure) and a fixed one (grey in the Figure). The moving one consists of two plates and four steel bars. The top and bottom plates are connected by four chrome finish steel bars 20 mm diameter and 2.5 mm thickness. The free span of these bars is 487 mm. These characteristics mean that they will each support more than 1000 N in buckling, which implies a safety factor sufficient for the experiments at hand. The dimensions of the top and bottom plates are 350 mm sides and 10 mm thickness, and the total mass of this moving mechanism is 10.488 kg. This part of the system is attached to the model, and it moves up and down freely, or forced when the actuator is attached to the bottom plate.

The fixed part of the system is the intermediate plate, which is clamped by two brackets to the main frame. The four air bushings are located approximately at the corners of the plate, wherein the chrome steel bars slide. The dimensions of this plate are 400 mm sides and 20 mm thickness. The actuator is attached to this plate at its centre.

A.3. Air bushings

One significant novelty of this system is the use of four air bushings (NewWay model S302001) that allow vertical motions of the moving part of the system with negligible friction (Figs. A.15 and A.16). Oil lubricated bearings could cause additional friction, which could lead to an increase in the measured damping. These bushings are 20 mm in diameter, and they need a 3.5–4.8 l/s air flow rate provided by an 8 bar compressor installed in the tank carriage.

The air bushings have to be robust enough to withstand lateral forces since heave plate models could produce flow asymmetries (see, e.g., Ref. (Tian et al., 2017)). The present ones allow a maximum lateral load of 133 N each, which leads to a substantial margin for the typical lateral hydrodynamic forces observed during the experiments presented herein. With these bushings, lateral motions and rotations are restrained, thus avoiding undesirable kinetic energy dissipation in motions other than heave.

Fig. A.16. Air bushings.

A.4. Load cell

The force signal is acquired with a single DoF load cell placed between the piston's actuator and the leg model. Depending on the range of the force to measure, the load cell can be changed. In the experiments carried out for this paper, the load cell model was an HBM U3, with a nominal range of ±500 N. This load cell is only necessary for forced oscillations. An image of the load cell used is shown in Fig. A.17.

A.5. Main frame

A frame of steel angular beams (UPN180 profiles) represents the interface between the tank carriage and the fixed part of the system. It creates a solid clamp that prevents any relative motions or rotations. Two diagonal reinforcements (UPN80 profiles) were added to increase its robustness, as can be appreciated in Fig. A.18. The aluminium fixed plate in Fig. A.15 is attached to this main frame with two angular brackets, also presented in Fig. A.18.

The design of the main frame allows flexibility to adjust the height of the mechanism with respect to the water surface. Anchor points along the vertical beams every 80 mm are available. The fine tuning of the vertical position below this 80 mm spacing is achieved by adjusting the filling level of the tank.

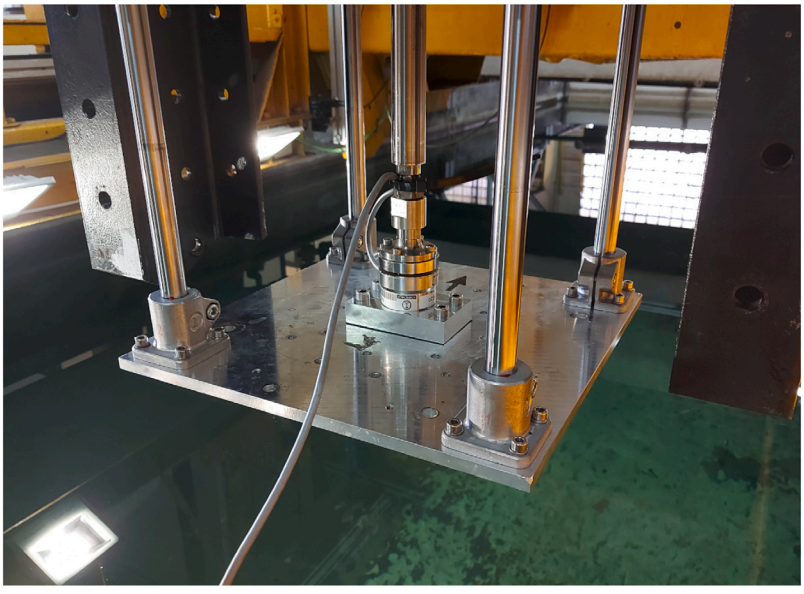

Fig. A.17. Single DoF load cell.

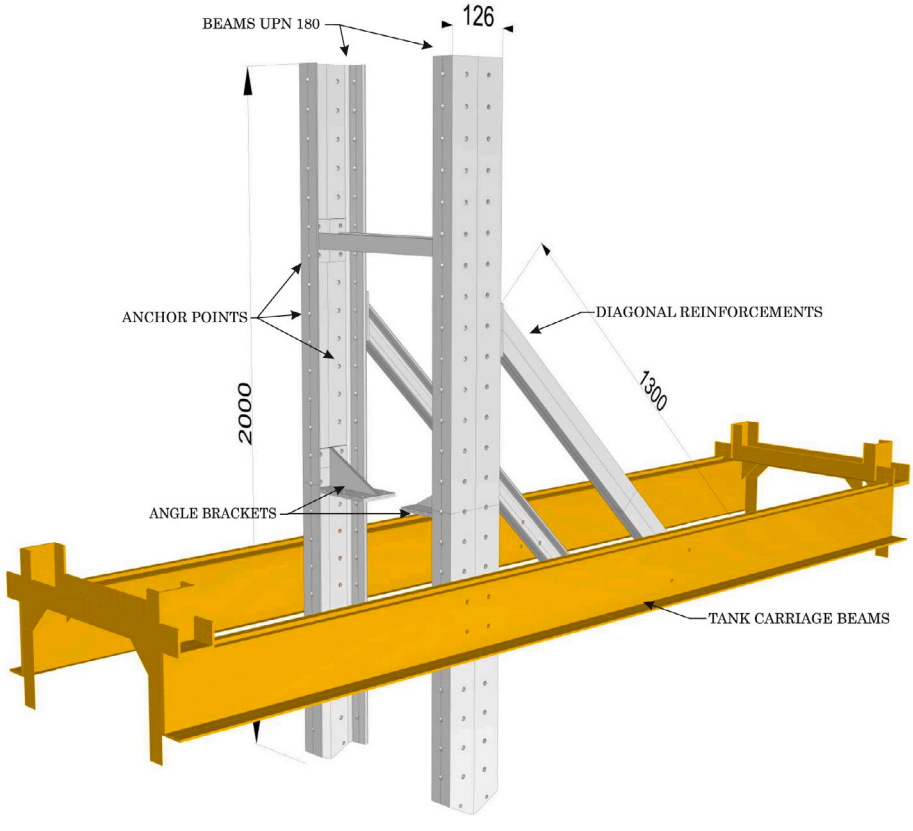

Fig. A.18. Main frame. UPN 180 and 80 profile beams clamped with the towing carriage (yellow). Vertical distributed holes are separated 80 mm between each. Dimensions in millimetres. (For interpretation of the references to colour in this figure legend, the reader is referred to the web version of this article.)

A.6. Laser

The vertical motions are measured with an external optical acquisition system when performing decay tests. The laser used is an Acuity (model AR500) with a range of 500 mm. Calibration of the laser was performed during the present work. It rendered a precision of ±0.1352 mm.

During the forced tests, the actuator encoder provides a redundant measurement of the position.

A.7. Acquisition system

For forced oscillation tests, the input motion signal is loaded into the actuator with a Labview script. The outputs, measured by the actuator's encoder and the load cell, are also processed by Labview.

The "National Instruments" acquisition system used is composed of a chassis module NI9174n, including a piezo-resistive channel card NI9237 for all sensors. This system is complemented by HBM hardware (Spider 8) and software (CATMAN) to record the laser position during free decay tests.

Appendix B. Experimental uncertainties

Following the ITTC general principles (ITTC, 2014a), the total uncertainties in $C^{KC}_{A_{33}}$ and $C^{KC}_{B_{33}}$ are obtained by propagating, according to Eq. (26), those of the parameters involved in such non-dimensional variables. Regarding added masses:

$$u^2(C^{KC}_{A_{33}}) = \left(\frac{1}{A_{33th}\ KC}\right)^2 u^2(A_{33}) + \frac{1}{KC^4}\left(\frac{A_{33}}{A_{33th}} - 1\right)^2 u^2(KC) + \frac{1}{KC^2}\left(\frac{A_{33}}{A^2_{33th}}\right)^2 u^2(A_{33th}). \tag{B.1}$$

In this equation the uncertainty in dimensional added mass $u\left(A_{33}\right)$ will be later discussed and the uncertainty in KC is:

$$u\left(KC\right) = \frac{2\pi}{D_d} u(z_0). \tag{B.2}$$

The uncertainties on model geometry and mass in the present case study can be considered negligible due to the shape of the model and its manufacturing accuracy. In addition, the water density uncertainty is comparatively negligible (see (ITTC, 2017, 2014b) for comparable examples in which this is the case). Since the uncertainties in the model geometry and mass, and the one in water density are the ones affecting $u(A_{33th})$ term in Eq. (B.1), this term will be considered negligible in what follows.

The total uncertainty (B.1) incorporates repetition related (A-type) and calibration (B-type) uncertainties, considered uncorrelated from the probabilistic point of view:

$$u^2\left(C^{KC}_{A_{33}}\right) = u^2_A\left(C^{KC}_{A_{33}}\right) + u^2_B\left(C^{KC}_{A_{33}}\right). \tag{B.3}$$

For each of these two terms, uncertainty propagation as in Eq. (B.1) is carried out. The one corresponding to the A-type uncertainties reads:

$$u^2_A(C^{KC}_{A_{33}}) = \left(\frac{1}{A_{33th}\ KC}\right)^2 u^2_A(A_{33}) + \frac{1}{KC^4}\left(\frac{A_{33}}{A_{33th}\ - 1}\right)^2 u^2_A(KC), \tag{B.4}$$

and the same applies to $u_B\left(C^{KC}_{A_{33}}\right)$.

In order to better understand the procedure to estimate all the terms above, let us take as example the particular forced oscillation case of the highest frequency and lowest KC ($\beta = 1108367$ and $KC = 0.0785$), starting with the A-type uncertainties.

B.1. A-type uncertainties

The A-type uncertainty is obtained from analysing the repeatability of the experiments, estimated from repeated measurements using the expression (ITTC, 2014a):

$$u_A\left(A_{33}\right) = \frac{\sigma_{A_{33}}}{\sqrt{N_{A_{33}}}}, \tag{B.5}$$

applied here to the added mass, with $\sigma_{A_{33}}$ being the standard deviation estimated from repeated tests and $N_{A_{33}}$ the number of tests. In our particular case, five repetitions for different selected KCs and motion frequencies have been done, and three repetitions of all decay tests.

Following (ITTC, 2014a), the standard deviation is obtained using the classic unbiased discrete estimator:

$$\sigma_{A_{33}} = \sqrt{\frac{1}{N_{A_{33}} - 1}\sum_{j=1}^{N_{A_{33}}}\left(A^j_{33} - \hat{A}_{33}\right)^2}, \tag{B.6}$$

with A^j_{33} the value of the added mass for each test, and $\hat{A}_{33}$ is the mean value of those A^j_{33}.

In the particular case of the proposed example, $A_{33} = 309.27$ kg, $\sigma_{A_{33}} = 1.104$ kg, $N_{A_{33}} = 5$, and therefore $u_A\left(A_{33}\right) = 0.494$ kg.

The same method is applied to obtain $u_A(z_0)$ (necessary to estimate $u_A(KC)$) and $u_A(\omega)$ (the latter will be necessary for the analysis of damping uncertainty).

A simplified method for obtaining A-type uncertainty for $C^{KC}_{A_{33}}$ is presented later in the paper, in Appendix B.5.

B.2. B-type uncertainties

Regarding the B-type uncertainty for the added mass in forced oscillations, it has to be borne in mind that the added mass is obtained from projecting the hydrodynamic force F_H onto the acceleration time history. In the hydrodynamic model, Eq. (3), let us denote $\hat{F_H}$ and $\hat{F}_{ext}$ as the amplitudes of the first harmonic of the hydrodynamic and measured forces, respectively, and let us denote ψ as the phase lag between F_{ext} and the time history of the motion $z(t)$. Considering this, one gets

$$A_{33} = \frac{1}{\omega^2}\left(\frac{\hat{F}_{ext}\cos(\psi)}{z_0} - C_{33}\right) - M. \tag{B.7}$$

By applying the propagation model (26) to estimate the B-type uncertainties in A_{33}, and by assuming uncertainties in M and C_{33} to be negligible, one gets:

$$u^2_B\left(A_{33}\right) = \frac{4}{\omega^6}\left(\frac{\hat{F}_{ext}\cos(\psi)}{z_0} - C_{33}\right)^2 u^2_B\left(\omega\right) + \frac{1}{\omega^4}\left(\frac{\cos(\psi)}{z_0}\right)^2 u^2_B\left(\hat{F}_{ext}\right) + \frac{1}{\omega^4}\left(\frac{\hat{F}_{ext}}{z_0}\right)^2 (\sin\psi)^2 u^2_B\left(\psi\right) + \frac{1}{\omega^4}\left(\frac{\hat{F}_{ext}\cos(\psi)}{z^2_0}\right)^2 u^2_B\left(z_0\right). \tag{B.8}$$

Regarding the frequency uncertainty, it is obtained from the sampling frequency (50 Hz for forced oscillations and 1 kHz for decay tests) as:

$$u_B(\omega) = \frac{2\pi}{T^2} u_B(T). \tag{B.9}$$

with T being the period, and with $u_B(T) = 0.02/\sqrt{3}$ s and $u_B(T) = 0.001/\sqrt{3}$ s for forced oscillations and decay tests respectively. The square root of 3 comes from assuming the probability distribution for the measurement to be uniform between ± 0.02 s and ± 0.001 s, respectively.

Regarding the force uncertainty, a one component load-cell HBM was used for the measurements, whose calibration line can be seen in Fig. B.19. The standard deviation of the residuals is taken as its B-type uncertainty:

$$u_B\left(\hat{F}_{ext}\right) = 0.034\,\text{N}. \tag{B.10}$$

Regarding the phase uncertainty, it can be considered negligible as force and motion are registered simultaneously in the same acquisition system.

Finally, regarding the uncertainty of heave amplitude motion, the laser measure system renders a standard deviation of ± 0.1352 mm in the residual values from its calibration, which leads to a B-type uncertainty of:

$$u_B\left(z_0\right) = 1.352 \cdot 10^{-4}\ \text{m}. \tag{B.11}$$

Collecting the terms together, one gets, for the considered example, $u_B\left(A_{33}\right) = 1.101$ kg.

In the case of decay tests, the B-type uncertainties are not connected to the force measurement but to the accuracy in the measurement of the time history (time and motion) during the decay process. A methodology for accounting for this type of uncertainty is provided in Appendix C.

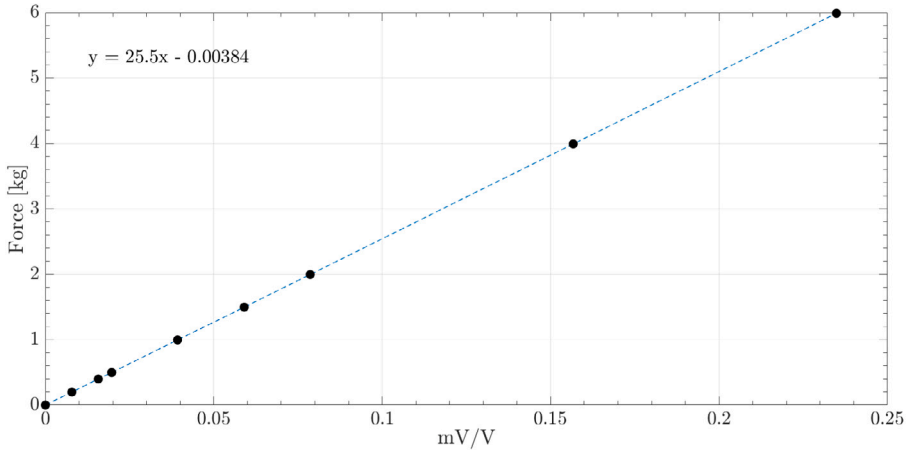

Fig. B.19. Calibration curve for single DOF load cell.

B.3. Total uncertainty

Adding all individual uncertainties in Eq. (B.1), $u\left(C^{KC}_{A_{33}}\right)$ is obtained. For the reference example,

$$u\left(C^{KC}_{A_{33}}\right) = 0.042,$$

with

$$C^{KC}_{A_{33}} = 0.249.$$

Following (ITTC, 2014a) the uncertainty $u\left(C^{KC}_{A_{33}}\right)$ should be multiplied by a coverage factor $k_p = 2$ for 95% confidence level, leading to the expanded uncertainty,

$$U\left(C^{KC}_{A_{33}}\right) = k_p\, u\left(C^{KC}_{A_{33}}\right) \tag{B.12}$$

equal to 0.084 for the reference example.

In Fig. B.20 the error bars with size equal to $U\left(C^{KC}_{A_{33}}\right)$ are included for a large number of forced oscillation tests, for which repetitions (specifically 5 repetitions) were available. The values of $C^{KC}_{A_{33}}$ coefficient for the decay tests are also presented in regards to the proposed added mass non-dimensionalization.

Regarding the decay tests values, a first observation is that the uncertainty cannot explain the dispersion found in these values. A second observation is that the uncertainties are higher for the lowest KC values. This is consistent with the fact that KC is in the denominator of formulas (27) and (28), which induces these large uncertainties in the very low KCs. In addition, the model of Eq. (27) assumes that the dimensionless added mass coefficient A'_{33} tends to be one in the low KC limit. Such assumption is based on an unbounded potential flow approximation to the theoretical added mass of a heaving disc, corrected to discount the effect of the central column. Even though such approximation works reasonably well, any deviations due to the actual viscous and free-surface bounded flow are largely amplified in the low KC range due to the fact that KC is in the denominator of $C^{KC}_{A_{33}}$. Regardless of this low KC behaviour, the continuity between decay and forced oscillation coefficients is noticeable.

The expanded relative uncertainty can be now computed as:

$$U'\left(C^{KC}_{A_{33}}\right) = \frac{U\left(C^{KC}_{A_{33}}\right)}{C^{KC}_{A_{33}}}, \tag{B.13}$$

equal to 0.335, i.e. 33.5% for the example chosen.

A summary of the results is included in Table B.2, providing the total expanded uncertainties $U\left(C^{KC}_{A_{33}}\right)$ for every case (as absolute and relative percentage values). The reference example is the first line. Its relative error is the highest due to the fact that its KC is the lowest one with the lowest frequency. In Table B.2, the contribution of A-type and B-type uncertainties in $U\left(C^{KC}_{A_{33}}\right)$ as a percentage over the total expanded uncertainty are also presented. As can be seen, A-type and B-type uncertainties are rather balanced. The contribution due to A_{33}, both the A and B-types, is the dominant one. This is shown in Tables B.3 and B.4.

B.4. Uncertainty of the modified damping coefficient $C^{KC}_{B_{33}}$

For the modified damping non-dimensional coefficient, $C^{KC}_{B_{33}}$, the followed methodology is analogous. However, in this case, the uncertainty in frequency must be taken into account as it appears in the denominator in such coefficient (Eq. (28)):

$$u^2(C^{KC}_{B_{33}}) = \left(\frac{1}{KC\ \omega\ A_{33th}}\right)^2 u^2(B_{33}) + \left(\frac{B_{33}-B_{330}}{KC^2\ \omega\ A_{33th}}\right)^2 u^2(KC) + \left(\frac{B_{33}-B_{330}}{KC\ \omega\ A^2_{33th}}\right)^2 u^2(A_{33th}) + \left(\frac{B_{33}-B_{330}}{KC\ \omega^2\ A_{33th}}\right)^2 u^2(\omega). \tag{B.14}$$

As for the $C^{KC}_{A_{33}}$ uncertainty, the $A_{33,th}$ contribution is neglected. For the B-type uncertainty of B_{33}, it has to be borne in mind that the damping is obtained from projecting the hydrodynamic force F_H onto the velocity time history. In the hydrodynamic model, Eq. (3), this implies that

$$B_{33} = \frac{\hat{F}_{ext}\sin(\psi)}{\omega\ z_0}. \tag{B.15}$$

Applying the propagation model (26) to Eq. (B.15), the B-type uncertainties in B_{33} is computed as:

$$u^2_B\left(B_{33}\right) = \left(\frac{\hat{F}_{ext}\sin(\psi)}{\omega^2\ z_0}\right)^2 u^2_B\left(\omega\right) + \left(\frac{\sin(\psi)}{\omega\ z_0}\right)^2 u^2_B\left(\hat{F}_{ext}\right) + \left(\frac{\hat{F}_{ext}\cos\psi}{\omega\ z_0}\right)^2 u^2_B\left(\psi\right) + \left(\frac{\hat{F}_{ext}\sin(\psi)}{\omega\ z_0^2}\right)^2 u^2_B\left(z_0\right). \tag{B.16}$$

Regarding the B-type frequency uncertainty for $u_B(\omega)$ see Eq. (B.9), for the force uncertainty $u_B\left(F_{ext}\right)$, see Eq. (B.10), and for the uncertainty in motion amplitude see Eq. (B.11). For the present analysis, the contribution of the phase uncertainty, $u_B(\psi)$, has been neglected since the motions and the forces were measured with the same acquisition system and sampling rate.

For the considered example, the expanded relative uncertainty is:

$$U'\left(C^{KC}_{B_{33}}\right) = \frac{U\left(C^{KC}_{B_{33}}\right)}{C^{KC}_{B_{33}}} = 0.131 \approx 13\%, \tag{B.17}$$

with the uncertainty being dominated by the B-type uncertainty in damping.

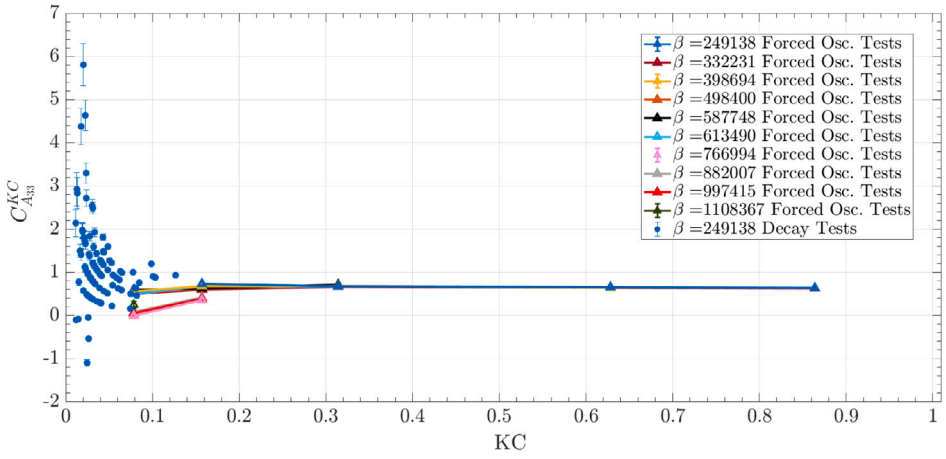

Fig. B.20. Total uncertainties for the modified added mass coefficient $C^{KC}_{A_{33}}$ computed with the propagation method described in Appendices B and C for forced oscillation and decay tests respectively.

Table B.2
Uncertainties for the modified added mass coefficient $C^{KC}_{A_{33}}$ computed with the propagation method described in Appendix B.

	$U\left(C^{KC}_{A_{33}}\right)$ [-]	$U'\left(C^{KC}_{A_{33}}\right)$ [%]	$u_A\left(C^{KC}_{A_{33}}\right)$ [-]	$u_B\left(C^{KC}_{A_{33}}\right)$ [-]	$u_A\left(C^{KC}_{A_{33}}\right)$ [%]	$u_B\left(C^{KC}_{A_{33}}\right)$ [%]
$KC = 0.078$	0.0837	33.5	0.0208	0.0363	36.4	63.6
$KC = 0.157$	0.0424	11.8	0.0206	0.0049	80.8	19.2
$KC = 0.314$	0.0170	5.7	0.0079	0.0031	71.6	28.4
$KC = 0.628$	0.0177	2.8	0.0052	0.0072	42.2	57.8
$KC = 0.866$	0.0155	2.3	0.0027	0.0073	27.4	72.6

Table B.3
Breakdown of A-type uncertainties for the modified added mass coefficient $C^{KC}_{A_{33}}$, for forced oscillation tests, displayed as percentages over the total A-type uncertainty $u_A\left(C^{KC}_{A_{33}}\right)$.

	$u_A\left(C^{KC}_{A_{33}}\right)$ [-]	$u_A\left(A_{33}\right)$ [%]	$u_A(KC)$ [%]
$KC = 0.078$	0.0208	99.2	0.8
$KC = 0.157$	0.0206	98.8	1.2
$KC = 0.314$	0.0079	98.9	1.1
$KC = 0.628$	0.0052	95.4	4.6
$KC = 0.866$	0.0027	97.6	2.4

Table B.4
Breakdown of B-type uncertainties for the modified added mass coefficient $C^{KC}_{A_{33}}$, for forced oscillation tests, displayed as percentages over the total B-type uncertainty $u_B\left(C^{KC}_{A_{33}}\right)$.

	$u_B\left(C^{KC}_{A_{33}}\right)$ [ ]	$u_B\left(A_{33}\right)$ [%]	$u_B(KC)$ [%]
$KC = 0.078$	0.0363	93.0	7.0
$KC = 0.157$	0.0049	70.1	29.9
$KC = 0.314$	0.0031	79.1	20.9
$KC = 0.628$	0.0072	89.4	10.6
$KC = 0.866$	0.0073	92.0	8.0

In Fig. B.21, the values of $C^{KC}_{B_{33}}$, with their uncertainties, are provided for all cases, including the decay experiments. Due to the change in steepness of damping coefficients obtained from decay tests and their offset in the ordinate axis, their values with this nondimensionalization differ radically from those obtained with forced oscillations. The continuity between them, is in any case, noticeable.

A summary of the results is included in Table B.5, providing the contributions of A-type and B-type uncertainties in $U\left(C^{KC}_{B_{33}}\right)$. As can be seen, B-type uncertainties are dominant (in most of them). Following Table B.6 the uncertainty of B_{33} is the largest one, compared to those of KC and ω over it. Nevertheless, the B-type uncertainty in frequency $u_B(\omega)$ is dominant in the calibration type uncertainties for damping coefficient as can be seen in Table B.7.

B.5. Alternative approach for estimating A-type uncertainty of the novel coefficients

The uncertainty $u(C^{KC}_{A_{33}})$ incorporates A-type and B-type contributions, as presented in Eq. (B.3). Both A-type and B-type uncertainties are obtained by propagating those of the variables on which the coefficient depends, as shown in Eq. (B.4) for the A-type uncertainty and what would be an analogous one for the B-type uncertainty.

This has been the approach followed in previous sections. However, considering the meaning of the A-type uncertainty, one could envision estimating its value for $C^{KC}_{A_{33}}$ directly from its variability, as:

$$u^{\sigma}_{A}\left(C^{KC}_{A_{33}}\right) := \frac{\sigma_{C^{KC}_{A_{33}}}}{\sqrt{N_{C^{KC}_{A_{33}}}}}, \tag{B.18}$$

which is a simpler approach. The same applies to $C^{KC}_{B_{33}}$. A justification for the practical equivalence to Eq. (B.4) of this approach is presented in Appendix D. Hence, the total uncertainties $U\left(C^{KC}_{A_{33}}\right)$ and $U\left(C^{KC}_{B_{33}}\right)$ can be calculated with Eq. (B.3) but using Eq. (B.18) for the A-type contribution.

Figs. B.22 and B.23 compare the total uncertainties for the coefficients obtained with the described in previous sections and the uncertainties computed by the alternative method described in the present section. Both for the added mass and hydrodynamic damping, the curves are superimposed, which justify that both methods are equivalent. The uncertainties are larger for the lowest KC cases, as previously anticipated in the paper. This is one of the reasons why the uncertainties in decay tests (see Appendix C) are significantly larger than those in forced oscillation tests.

The standard deviation uncertainty estimates, as used in Figs. 7–12 for A'_{33} and B'_{33}, are also included. They are not in principle comparable to the uncertainties as they intend to describe the dispersion of the experimental measurements, compared to the uncertainties themselves, which aim to define confidence interval for the mean values of such experimental measurements. The A components of such uncertainties are obtained from the standard deviations but reduced with the square

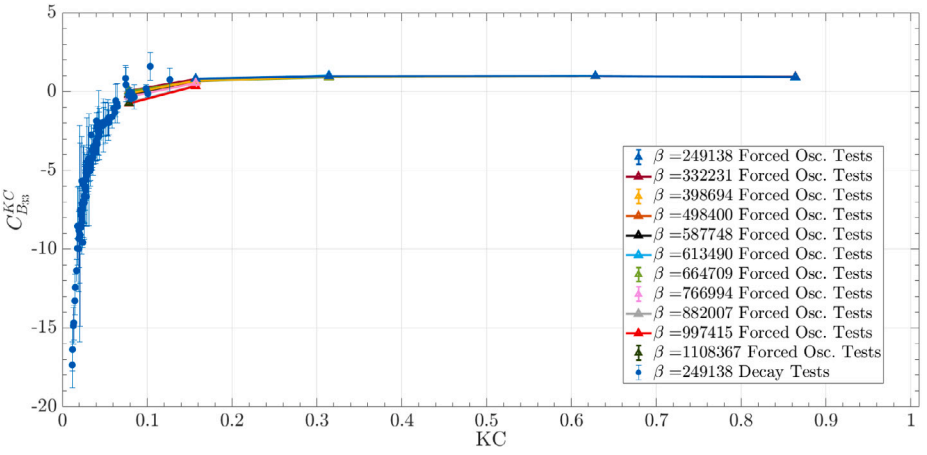

Fig. B.21. Total uncertainties for the modified added mass coefficient $C^{KC}_{B_{33}}$ computed with the propagation method described in Appendix B.4 and as in Appendix C for forced oscillation and decay tests, respectively.

Table B.5
Uncertainties for the modified damping coefficient $C^{KC}_{B_{33}}$ computed for forced oscillation tests, with the propagation method described in Appendix B.4.

	$U\left(C^{KC}_{B_{33}}\right)$ [-]	$U'\left(C^{KC}_{B_{33}}\right)$ [%]	$u_A\left(C^{KC}_{B_{33}}\right)$ [-]	$u_B\left(C^{KC}_{B_{33}}\right)$ [-]	$u_A\left(C^{KC}_{B_{33}}\right)$ [%]	$u_B\left(C^{KC}_{B_{33}}\right)$ [%]
$KC = 0.078$	0.0969	13.1	0.0274	0.0399	40.7	59.3
$KC = 0.157$	0.0472	8.8	0.0090	0.0218	29.1	70.9
$KC = 0.314$	0.0280	3.1	0.0025	0.0138	15.1	84.9
$KC = 0.628$	0.0183	1.9	0.0073	0.0056	56.4	43.6
$KC = 0.866$	0.0226	2.5	0.0107	0.0037	74.5	25.5

Table B.6
Breakdown of A-type uncertainties for the modified damping coefficient $C^{KC}_{B_{33}}$ for forced oscillation tests, displayed as percentages over the total A-type uncertainty $u_A\left(C^{KC}_{B_{33}}\right)$.

	$u_A\left(C^{KC}_{B_{33}}\right)$ [-]	$u_A\left(B_{33}\right)$ [%]	$u_A(KC)$ [%]	$u_A(\omega)$ [%]
$KC = 0.078$	0.0274	94.3	5.5	0.2
$KC = 0.157$	0.0090	85.8	13.9	0.2
$KC = 0.314$	0.0025	81.3	17.8	0.9
$KC = 0.628$	0.0073	92.3	7.1	0.6
$KC = 0.866$	0.0107	98.1	1.2	0.8

Table B.7
Breakdown of B-type uncertainties for the modified damping coefficient $C^{KC}_{B_{33}}$ for forced oscillation tests, displayed as percentages over the total A-type uncertainty $u_B\left(C^{KC}_{B_{33}}\right)$.

	$u_B\left(C^{KC}_{B_{33}}\right)$ [-]	$u_B\left(B_{33}\right)$ [%]	$u_B(KC)$ [%]	$u_B(\omega)$ [%]
$KC = 0.078$	0.0399	9.7	41.3	49.0
$KC = 0.157$	0.0218	8.2	34.7	57.1
$KC = 0.314$	0.0138	8.2	23.8	68.0
$KC = 0.628$	0.0056	7.3	24.1	68.6
$KC = 0.866$	0.0037	8.0	23.4	68.7

root of the number of samples (see Eq. (B.5)). Even with this reduction, the standard deviation values are generally smaller than the total uncertainties (A plus B) computed with the techniques studied in these appendices.

Appendix C. B-type uncertainties of added mass and damping during decay tests

C.1. B-type uncertainties of added mass during decay tests

The added mass, A_{33}, can be estimated from decay tests using Eq. (20). With this model, its B-type uncertainty can be computed by propagating those in C_{33}, M and $\omega_{3,eq,i}$. Since the former two are properties connected to precision in the manufacture of the model, they are negligible compared to the latter.

The undamped natural frequency in cycle i, $\omega_{3,eq,i}$, is obtained itself with Eq. (17), and therefore, its B-type uncertainty will be a function of the damped frequency $\omega_{3,d,i}$ and the equivalent linear damping coefficient $\mu_{eq,i}$. But first let us expressed it in terms of its uncorrelated primitive variables. The damped frequency $\omega_{3,d,i}$ is obtained directly from the damped period $T_{d,i} = 2\left(t_{i+1} - t_i\right)$ measured from the time history, and the equivalent linear damping coefficient, $\mu_{eq,i}$, is obtained by fitting two consecutive peaks of the ith half cycle of a decay time history with Eq. (16), which gives us Eq. (19). Then $\omega_{3,eq,i}$ leads:

$$\omega_{3,eq,i} = \sqrt{\omega^2_{3,d,i} + \mu^2_{eq,i}} \overset{(18)(19)}{=} \sqrt{\left(\frac{2\pi}{T_{d,i}}\right)^2 + \left(\frac{2\log\left(\frac{|Z_i|}{|Z_{i+1}|}\right)}{T_{d,i}}\right)^2}$$
$$= \frac{2\pi}{T_{d,i}}\sqrt{1 + \left(\frac{\log\left(\frac{|Z_i|}{|Z_{i+1}|}\right)}{\pi}\right)^2}$$
$$= \frac{2\pi}{T_{d,i}}\sqrt{1 + \left(\frac{\lambda_i}{\pi}\right)^2}, \tag{C.1}$$

with $\lambda_i = \log\left(\frac{|Z_i|}{|Z_{i+1}|}\right)$. Therefore, its B-type uncertainty is:

$$u^2_B\left(\omega_{3,eq,i}\right) = \left(\frac{2\pi}{T^2_{d,i}}\right)^2 \left(1 + \left(\frac{\lambda_i}{\pi}\right)^2\right) u^2_B\left(T_{d,i}\right) +$$
$$\left(\frac{2\pi}{T_{d,i}} \frac{\lambda_i/\pi^2}{\sqrt{1 + (\lambda/\pi)^2}}\right)^2 u^2_B(\lambda_i)$$
$$= \left(\frac{\omega_{3,eq,i}}{T_{d,i}}\right)^2 u^2_B\left(T_{d,i}\right) + \left(\omega_{3,eq,i} \frac{\lambda_i/\pi^2}{1 + (\lambda_i/\pi)^2}\right)^2 u^2_B(\lambda_i) \tag{C.2}$$

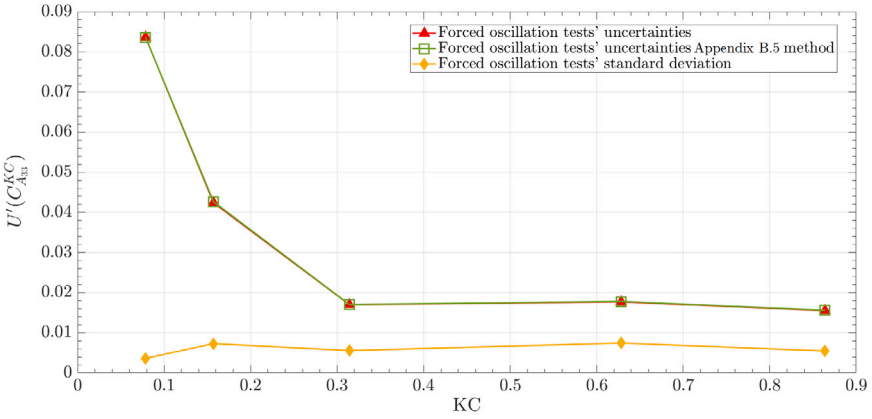

Fig. B.22. Added mass coefficients' total uncertainties computed by propagation method described in Appendix B (see Eq. (B.4)) and by the alternative approach method described in Appendix B.5 (see Eq. (B.18)).

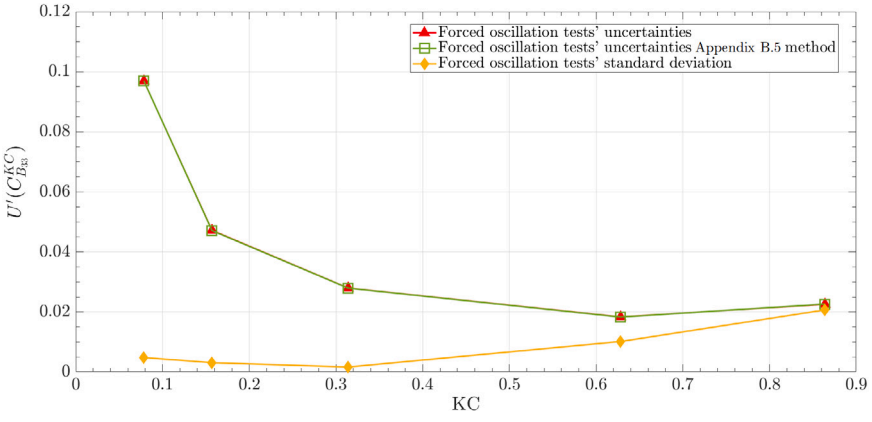

Fig. B.23. Damping coefficients' total uncertainties computed by propagation method described in Appendix B and by the alternative approach method described in Appendix B.5.

The sampling frequency in the decay tests is 1 Khz, and therefore

$$u_B\left(T_{d,i}\right) = 2\sqrt{2}\,\frac{0.001}{\sqrt{3}}\ s, \tag{C.3}$$

if a uniform probability distribution is assumed for this variable and assuming same uncertainty for t_i and t_{i+1}, then

$$u_B^2\left(\lambda_i\right) = \left(\left(\frac{1}{|Z_i|}\right)^2 + \left(\frac{1}{|Z_{i+1}|}\right)^2\right) u_B^2\left(z_0\right). \tag{C.4}$$

Finally, propagating uncertainties with Eq. (20), one gets:

$$u_B(A_{33}) = 2\frac{C_{33}}{\omega^3_{3,eq,i}}\, u_B\left(\omega_{3,eq,i}\right). \tag{C.5}$$

C.2. B-type uncertainties of damping during decay tests

For the damping coefficient, $B_{eq,33,i}$, obtained from Eq. (21), it needs to be expressed in terms of primitive measured variables:

$$\begin{aligned} B_{eq,33,i} &= 2\eta_i\sqrt{\left(M + A_{33,i}\right)C_{33}} \\ &\overset{(20)(22)}{=} 2\frac{\mu_{eq,i}}{\omega_{3,eq,i}}\sqrt{\left(M + \frac{C_{33}}{\omega^2_{3,eq,i}} - M\right)C_{33}} \\ &= 2\frac{\mu_{eq,i}}{\omega^2_{3,eq,i}}\, C_{33} \\ &\overset{(18)}{=} 2\frac{\mu_{eq,i}}{\omega^2_{3,d,i} + \mu^2_{eq,i}}\, C_{33}. \end{aligned} \tag{C.6}$$

From Eqs. (17) and (19) and remembering that $T_{d,i} = 2\left(t_{i+1} - t_i\right)$, the damping $B_{eq,33,i}$ can be expressed as

$$B_{eq,33,i} = 2\frac{\frac{2}{T_{d,i}}\log\left(\frac{|Z_i|}{|Z_{i+1}|}\right)}{\frac{4\pi^2}{T^2_{d,i}} + \frac{4}{T^2_{d,i}}\log^2\left(\frac{|Z_i|}{|Z_{i+1}|}\right)}C_{33} = \frac{T_{d,i}\ \lambda_i\ C_{33}}{\pi^2 + \lambda_i^2}. \tag{C.7}$$

Now its B-type uncertainty propagation can be carried out, neglecting the C_{33} and mass contributions, computed as:

$$\begin{aligned} u_B^2\left(B_{eq,33,i}\right) &= \left(\frac{C_{33}\lambda_i}{\pi^2 + \lambda_i^2}\right)^2 u_B^2\left(T_{d,i}\right) + \left(C_{33}T_{d,i}\frac{\pi^2 - \lambda_i^2}{\left(\pi^2 + \lambda_i^2\right)^2}\right)^2 u_B^2\left(\lambda_i\right) \\ &= \left(\frac{B_{eq,33,i}}{T_{d,i}}\right)^2 u_B^2\left(T_{d,i}\right) + \left(B_{eq,33,i}\frac{\pi^2 - \lambda_i^2}{\pi^2 + \lambda_i^2}\frac{1}{\lambda_i}\right)^2 u_B^2\left(\lambda_i\right). \end{aligned} \tag{C.8}$$

The B-type uncertainty for $T_{d,i}$ is already known with Eq. (C.3) and $u_B^2\left(\lambda_i\right)$ is computed with Eq. (C.4).

Appendix D. Discussion on the alternative method for estimating $u_A\left(C^{KC}_{A_{33}}\right)$

In this appendix, the practical equivalence of the estimates of $u_A\left(C^{KC}_{A_{33}}\right)$ in Eqs. (B.4) and (B.18) is shown.

Let us expand the coefficient $C^{KC}_{A_{33}}$ for small perturbations around their mean of the variables on which it depends, retaining only the first

order terms:

$$C^{KC}_{A_{33}}\left(\overline{A}_{33}+\Delta A_{33},\overline{A}_{33,th}+\Delta A_{33,th},\overline{KC}+\Delta KC\right)=\frac{\partial C^{KC}_{A_{33}}}{\partial A_{33}}\Delta A_{33}+\frac{\partial C^{KC}_{A_{33}}}{\partial A_{33,th}}\Delta A_{33,th}+\frac{\partial C^{KC}_{A_{33}}}{\partial KC}\Delta KC. \quad (D.1)$$

Assuming these perturbations to be uncorrelated, the variance of $C^{KC}_{A_{33}}$ can be obtained as:

$$\sigma^2(C^{KC}_{A_{33}})=\left(\frac{\partial C^{KC}_{A_{33}}}{\partial A_{33}}\right)^2\sigma^2(A_{33})+\left(\frac{\partial C^{KC}_{A_{33}}}{\partial A_{33,th}}\right)^2\sigma^2(A_{33,th})+\left(\frac{\partial C^{KC}_{A_{33}}}{\partial KC}\right)^2\sigma^2(KC). \quad (D.2)$$

If the repetitions used to estimate all the variances are the same, we can divide the previous equation by such number N to obtain:

$$\left(u^{\sigma}_{A}(C^{KC}_{A_{33}})\right)^2=\left(\frac{\partial C^{KC}_{A_{33}}}{\partial A_{33}}\right)^2u^2_A(A_{33})+\left(\frac{\partial C^{KC}_{A_{33}}}{\partial A_{33,th}}\right)^2u^2_A(A_{33,th})+\left(\frac{\partial C^{KC}_{A_{33}}}{\partial KC}\right)^2u^2_A(KC). \quad (D.3)$$

Assuming, as discussed in Appendix B, that the uncertainties of $A_{33,th}$ are negligible, the right hand side of this equation is precisely $u^2_A(C^{KC}_{A_{33}})$ as estimated from Eq. (B.4). This justifies the practical equivalence of the estimates of $u_A\left(C^{KC}_{A_{33}}\right)$ in Eqs. (B.4) and (B.18), on the basis of small perturbations of the variables in place with respect to their means. The same applies to $u_A\left(C^{KC}_{B_{33}}\right)$.

References

Anglada-Revenga, E., Bezunartea-Barrio, A., Maron-Loureiro, A., Molinelli-Fernandez, E., Oria-Escudero, J., Saavedra-Ynocente, L., Soriano-Gomez, C., Duque-Campayo, D., Gomez-Goni, J., Souto-Iglesias, A., 2020. Scale effects in heave plates: PIV investigation. In: International Conference on Offshore Mechanics and Arctic Engineering. vol. 84416, American Society of Mechanical Engineers, V009T09A061.

Bachynski, E.E., Moan, T., 2012. Design considerations for tension leg platform wind turbines. Marine Struct. 29 (1), 89–114. http://dx.doi.org/10.1016/j.marstruc.2012.09.001, https://www.sciencedirect.com/science/article/pii/S0951833912000627.

Bezunartea-Barrio, A., Fernandez-Ruano, S., Maron-Loureiro, A., Molinelli-Fernandez, E., Moreno-Buron, F., Oria-Escudero, J., Rios-Tubio, J., Soriano-Gomez, C., Valea-Peces, A., Lopez-Pavon, C., Souto-Iglesias, A., 2019. Scale effects on heave plates for semi-submersible floating offshore wind turbines: Case study with a solid plain plate. J. Offshore Mech. Arct. Eng. 142 (3), 031105. http://dx.doi.org/10.1115/1.4045374.

Bulian, G., Francescutto, A., Fucile, F., 2009. Determination of Relevant Parameters for the Alternative Assessment of Intact Stability Weather Criterion On Experimental Basis. Project Report. Tech. rep., EU-funded Project HYD-III-CEH-5 (Integrated Infrastructure Initiative HYDRALAB III, Contract no. 022441 (RII3)), Department DINMA, University of Trieste, Via A. Valerio 10, 34127, Trieste, Italy.

do Carmo, L.H.S., de Mello, P.C., Malta, E.B., Franzini, G.R., Simos, A.N., Gonçalves, R.T., Suzuki, H., 2020. In: ASME (Ed.), Analysis of a FOWT Model in Bichromatic Waves: An Investigation on the Effect of Combined Wave-Frequency and Slow Motions on the Calibration of Drag and Inertial Force Coefficients. In: Volume 9: Ocean Renewable Energy of International Conference on Offshore Mechanics and Arctic Engineering, V009T09A047. http://dx.doi.org/10.1115/OMAE2020-18239.

Garrido-Mendoza, C., Thiagarajan, K., Souto-Iglesias, A., Colagrossi, A., Bouscasse, B., 2015. Computation of flow features and hydrodynamic coefficients around heave plates oscillating near a seabed. J. Fluids Struct. 59, 406–431. http://dx.doi.org/10.1016/j.jfluidstructs.2015.10.003.

Goupee, A.J., Koo, B.J., Kimball, R.W., Lambrakos, K.F., Dagher, H.J., 2014. Experimental comparison of three floating wind turbine concepts. J. Offshore Mech. Arct. Eng. 136 (2), 020906. http://dx.doi.org/10.1115/1.4025804.

Gueydon, S., Weller, S., 2013. Study of a floating foundation for wind turbines. J. Offshore Mech. Arct. Eng. 135 (3), 031903. http://dx.doi.org/10.1115/1.4024271.

ITTC, 2014a. International Towing Tank Conference, Guide to the Expression of Uncertainty in Experimental Hydrodynamics, Report 7.5-02-01-01, Revision 02. Tech. rep., ITTC.

ITTC, 2014b. International Towing Tank Conference, Recommended Procedures and Guidelines: Example for Uncertainty Analysis of Resistance Tests in Towing Tanks, Report 7.5-02-02-02.1. Tech. rep., ITTC.

ITTC, 2017. International Towing Tank Conference, ITTC Quality System Manual, Recommended Procedures and Guidelines, Guideline to Practical Implementation of Uncertainty Analysis, Report 7.5-02-01-07. Tech. rep., ITTC.

Li, J., Liu, S., Zhao, M., Teng, B., 2013. Experimental investigation of the hydrodynamic characteristics of heave plates using forced oscillation. Ocean Eng. 66 (0), 82–91.

Liu, Y., Hu, C., Sueyoshi, M., Yoshida, S., Iwashita, H., Kashiwagi, M., 2021. Motion response characteristics of a Kyushu-University semi-submersible floating wind turbine with trussed slender structures: experiment vs. numerical simulation. Ocean Eng. 232, 109078. http://dx.doi.org/10.1016/j.oceaneng.2021.109078, https://www.sciencedirect.com/science/article/pii/S0029801821005138.

Liu, Y., Yoshida, S., Yamamoto, H., Toyofuku, A., HE, G., Yang, S.-H., 2018. Response characteristics of the deepcwind floating wind turbine moored by a single-point mooring system. Appl. Sci. 8, 2306. http://dx.doi.org/10.3390/app8112306.

Lopez-Pavon, C., Souto-Iglesias, A., 2015. Hydrodynamic coefficients and pressure loads on heave plates for semi-submersible floating offshore wind turbines: A comparative analysis using large scale models. Renew. Energy 81 (0), 864–881. http://dx.doi.org/10.1016/j.renene.2015.04.003, http://www.sciencedirect.com/science/article/pii/S0960148115002839.

Mentzoni, F., Kristiansen, T., 2020. Two-dimensional experimental and numerical investigations of perforated plates in oscillating flow, orbital flow and incident waves. Appl. Ocean Res. 97, 102078. http://dx.doi.org/10.1016/j.apor.2020.102078, https://www.sciencedirect.com/science/article/pii/S0141118719307060.

Robertson, A., Bachynski, E.E., Gueydon, S., Wendt, F., Schünemann, P., 2020. Total experimental uncertainty in hydrodynamic testing of a semisubmersible wind turbine, considering numerical propagation of systematic uncertainty. Ocean Eng. 195, 106605. http://dx.doi.org/10.1016/j.oceaneng.2019.106605, http://www.sciencedirect.com/science/article/pii/S0029801819307309.

Robertson, A.N., Bachynski, E.E., Gueydon, S., Wendt, F., Schünemann, P., Jonkman, J., 2018. Assessment of experimental uncertainty for a floating wind semisubmersible under hydrodynamic loading. In: ASME (Ed.), Volume 10: Ocean Renewable Energy of International Conference on Offshore Mechanics and Arctic Engineering. V010T09A076. http://dx.doi.org/10.1115/OMAE2018-77703.

Saettone, S., Molinelli, E., Fernández, C., Saavedra, L., Duque, D., Souto-Iglesias, A., Maron, A., 2021. A PIV investigation of the flow close to a heave plate of a semi-submersible floating wind turbine for models of diferent scales. [Submitted for publication].

Sarpkaya, T., Isaacson, M., 1981. Mechanics of wave forces on offshore structures. van Nostrand Reinhold, New York.

Simos, A.N., Ruggeri, F., Watai, R.A., Souto-Iglesias, A., Lopez-Pavon, C., 2018. Slow-drift of a floating wind turbine: An assessment of frequency-domain methods based on model tests. Renew. Energy 116 (Part A), 133–154. http://dx.doi.org/10.1016/j.renene.2017.09.059, http://www.sciencedirect.com/science/article/pii/S0960148117309229.

Tao, L., Dray, D., 2008. Hydrodynamic performance of solid and porous heave plates. Ocean Eng. 35 (10), 1006–1014. http://dx.doi.org/10.1016/j.oceaneng.2008.03.003.

Tao, L., Molin, B., Scolan, Y.-M., Thiagarajan, K., 2007. Spacing effects on hydrodynamics of heave plates on offshore structures. J. Fluids Struct. 23 (8), 1119–1136. http://dx.doi.org/10.1016/j.jfluidstructs.2007.03.004.

Thiagarajan, K., Moreno, J., 2020. Wave induced effects on the hydrodynamic coefficients of an oscillating heave plate in offshore wind turbines. J. Marine Sci. Eng. 8 (8), http://dx.doi.org/10.3390/jmse8080622, https://www.mdpi.com/2077-1312/8/8/622.

Thiagarajan, K.P., Troesch, A.W., 1994. Hydrodynamic heave damping estimation and scaling for tension leg platforms. J. Offshore Mech. Arct. Eng. 116 (2), 70–76.

Tian, X., Xiao, L., Zhang, X., Yang, J., Tao, L., Yang, D., 2017. Flow around an oscillating circular disk at low to moderate Reynolds numbers. J. Fluid Mech. 812, 1119–1145. http://dx.doi.org/10.1017/jfm.2016.800.

Uzunoglu, E., Guedes Soares, C., 2020. Hydrodynamic design of a free-float capable tension leg platform for a 10 mw wind turbine. Ocean Eng. 197, 106888. http://dx.doi.org/10.1016/j.oceaneng.2019.106888.

Wadhwa, H., Krishnamoorthy, B., Thiagarajan, K.P., 2010. Variation of heave added mass and damping near seabed. In: ASME (Ed.), ASME 29th International Conference on Offshore Mechanics and Arctic Engineering, OMAE. In: Vol. 29th International Conference on Ocean, Offshore and Arctic Engineering: Volume 1 of International Conference on Offshore Mechanics and Arctic Engineering, pp. 271–277. http://dx.doi.org/10.1115/OMAE2010-20456.